Multiscale and Multidisciplinary Modeling, Experiments and Design (2026) 9:10
https://doi.org/10.1007/s41939-025-01082-w

ORIGINAL PAPER

Performance analysis of concrete-filled aluminum tubes confined with aramid fiber sheets under axial loading: a combined numerical and machine learning approach

Diyar N. Qader[1] · Saif Alzabeebee[2,3] · Amirreza Kandiri[4] · Pshtiwan Shakor[5] · Sarkawt Saeed[5] · Rwayda Kh. S. Al-Hamd[6,7]

Received: 22 September 2025 / Revised: 13 October 2025 / Accepted: 16 October 2025
© The Author(s) 2025

Abstract

This study presents a comprehensive investigation into the axial performance of concrete-filled aluminum tubular (CFAT) columns externally confined with aramid fiber-reinforced polymer (AFRP) sheets, using an integrated finite element analysis (FEA) and machine learning (ML) framework. While CFAT columns offer significant advantages such as reduced weight, high corrosion resistance, and architectural appeal, their structural performance is often limited by the lower stiffness and yield strength of aluminum. To overcome these limitations, this research explores the use of AFRP confinement to enhance load-bearing capacity and ductility. A validated FEA model was developed in ABAQUS based on 23 experimental CFAT stub column tests, showing strong agreement with results (where PEXP/PFEA, the ratio of experimental to FEA-predicted load capacities, ranged from 0.85 to 1.14, confirming model accuracy). A detailed parametric analysis investigated the effects of AFRP layer count, concrete strength, and tube geometry (D/t ratio, the diameter-to-thickness ratio indicating slenderness), revealing that AFRP confinement significantly improves performance—particularly in thin-walled columns. Additionally, four ML models (SVR, RF, ANN, Meta-ANN) were trained on 113 datasets generated from numerical simulations to predict ultimate axial load capacity. The Meta-ANN model achieved the highest accuracy with a MAPE of 2.02% and R of 0.99. To interpret the predictions, SHAP (SHapley Additive exPlanations) analysis was used, identifying column diameter and concrete strength as the most influential parameters. This dual numerical–data-driven approach demonstrates the potential of combining AFRP confinement with AI-based prediction tools for the design and optimization of advanced composite columns.

Keywords Concrete-filled aluminum tubes (CFAT) · Aramid fiber-reinforced polymer (AFRP) · Axial load capacity · Finite element analysis (FEA) · Machine learning models

✉ Rwayda Kh. S. Al-Hamd
r.al-hamd@abertay.ac.uk; rwayda.alhamd@gmail.com

Diyar N. Qader
diyar.nasih@uokirkuk.edu.iq

Saif Alzabeebee
saif.alzabeebee@qu.edu.iq

[1] Civil Engineering Department, University of Kirkuk, Kirkuk 36001, Iraq

[2] Department of Roads and Transport Engineering, University of Al-Qadisiyah, Al Diwaniyah 58002, Iraq

[3] College of Engineering, University of Warith Al-Anbiyaa, Karbala 56001, Iraq

[4] School of Civil Engineering, University College Dublin, Dublin, Ireland

[5] Technical College of Engineering, Sulaimani Polytechnic University, Sulaymaniyah 46001, Iraq

[6] Department of Built Environment and Life Sciences, Faculty of Social and Applied Sciences , Abertay University, Dundee DD1 1HG, Scotland, UK

[7] Department of Civil Engineering and Management, Faculty of Science and Engineering, The University of Manchester, Manchester, M13 9PL, England, United Kingdom

Published online: 25 October 2025

1 Introduction

Concrete-filled aluminum tubular (CFAT) columns have attracted extensive interest in contemporary structural engineering owing to the unique synergism of properties, such as lightweight characteristic, high corrosion resistance, and aesthetic sensibility. As a result of these attributes, CFAT columns are especially well-suited for use in high-rise structures, long-span bridges, and offshore structures, where weight savings and durability are fundamental design objectives (Ding et al. 2021; Zhou and Young 2008; Yan et al. 2024a, 2024b; Rong et al. 2023; Qader et al. 2024; Hakeem et al. 2024). Through a composite action between the aluminum alloy tube and infilled concrete, the structural performance of a CFAT column in axial compression is significantly improved with effective confinement provided to the concrete core. This leads to not only an increase in the overall capacity but also a decrease in the local buckling of the aluminum tube, a common failure mechanism of thin-walled metallic components (Zhou and Young 2009; Mi et al. 2024; Jiang et al. 2024a; Saha et al. 2024; Mansour et al. 2024a). On the other hand, one of the main problems related to CFAT columns are the lower elastic modulus and yield strength of aluminum alloys compared to conventional steel. This limitation has a direct impact on the confinement effect provided by the aluminum tube, which can reduce the axial load capacity and overall ductility of the system (Ding et al. 2021; Yan et al. 2024c; Lu et al. 2024; Al-Rousan et al. 2024). Therefore, researchers have proposed several techniques to strengthen CFAT columns, and the application of fiber-reinforced polymer (FRP) composites is one of the most effective methods due to their high strength-to-weight ratios, excellent corrosion-resistance properties, and convenient operation (Mansour et al. 2024b, 2022; Wang et al. 2020; Wang et al. 2025; Jiang et al. 2024b; Yue, et al. 2024; Al-Rousan et al. 2022).

Several studies have explored the behavior of aluminum structural columns under axial load. Zhu and Young (2006) investigated fixed-ended aluminum tubular columns with square and rectangular hollow sections, identifying the effects of transverse welds and heat-affected zones (HAZ) on performance through experiments and finite element analysis (FEA). Extending this work, Zhou and Young (2009) examined concrete-filled aluminum circular hollow section (CHS) columns and found that composite interaction between the tube and concrete markedly enhances strength and stiffness, particularly at low D/t ratios. They also noted that design codes such as American and Australian/New Zealand standards tend to produce conservative predictions. Similarly, Ellobody et al. (2006) compared various design codes for concrete-filled steel tube columns, concluding that while US and Australian provisions were conservative, the European code tended to be unconservative. Zhou and Young (2012, 2018) further refined their studies by developing design equations for single and double-skin aluminum CHS columns, revealing that dual-tube configurations significantly improve stability and ultimate capacity.

Other researchers have examined strengthening strategies and material effects. Wang et al. (2023) reported that CFRP wrapping enhanced the axial strength and ductility of aluminum tube columns by up to 30.8% and 43.4%, respectively. Ding et al. (2021) confirmed that confinement by aluminum tubes is less effective than steel due to aluminum's lower modulus of elasticity but proposed an analytical design formula for accurate strength prediction. Yan et al. (2023) introduced a fiber-element model for double-skin aluminum tubes with high-strength concrete, achieving improved strength but reduced ductility. Mansour et al. (2024b) focused on FRP-strengthened CFST columns, demonstrating that FRP confinement delayed buckling and increased cyclic energy dissipation. Collectively, these studies underscore that composite action significantly enhances load capacity, stiffness, and ductility, and that parameters such as material type and geometry are critical in defining column performance.

As a high-performance composite, aramid fiber-reinforced polymer (AFRP) has gained attention for its superior tensile strength, impact resistance, and energy absorption properties (Li et al. 2020; Zhang et al. 2023; Al-Rousan 2020; Al-Rousan and Barfed 2019; Al-Rousan and Bara'a 2025; Al-Sulayvani and Al-Talabani 2015). Previous studies on AFRP-confined CFST columns confirmed substantial gains in axial strength, ductility, and energy dissipation (Wang et al. 2020; Zhang et al. 2023; Al-Rousan and Alnemrawi 2023; Al-Rousan 2022). However, its application to CFAT columns remains largely unexplored. The mechanical differences between aluminum and steel—especially in stiffness and yield stress—affect the confinement mechanism and overall structural behavior. Most existing FRP confinement models have been developed from steel tube systems, and their direct use for aluminum tubes may lead to inaccuracies. Therefore, additional experimental, numerical, and analytical investigations are required to better understand AFRP-strengthened CFAT columns, identify their confinement mechanisms, and develop reliable design correlations.

Recent research has placed growing emphasis on the use of FRP composites and sustainable materials for strengthening and improving the performance of concrete structures (Al-Rousan and Barfed 2019; Al-Rousan and Alnemrawi 2023; Al-Rousan 2022; Fediuk et al. 2023; Abdalla et al. 2020). Suparp et al. (2023) examined the behavior of non-prismatic reinforced concrete beams reinforced with green GFRP rebars, highlighting their potential for enhancing mechanical performance while reducing environmental impact in sustainable infrastructure. Similarly, Thansirichaisree et al.

(2024) investigated the stress–strain behavior of square concrete columns confined with hybrid B-CSM composites, developing new predictive models that revealed superior strength and ductility in hybrid confinement systems compared to traditional FRP configurations. Furthermore, Yooprasertchai et al. (2024) demonstrated that using treated and untreated plastic waste aggregates can significantly enhance the sustainability of concrete without compromising strength, while Saingam et al. (2025) studied the incorporation of recycled electronic waste fibers and recycled glass aggregates into self-consolidating mortar to improve mechanical and durability properties. In addition, Farooq et al. (2024) emphasized the use of pumice powder combined with hybrid fibers as a sustainable additive to improve concrete performance. Collectively, these studies underscore the importance of developing environmentally friendly materials and reinforcement strategies to achieve structural efficiency and sustainability.

In addition to conventional experimental and numerical methodologies, incorporating machine learning (ML) techniques has become a game changer in the field of structural engineering which has the potential to generate groundbreaking results for predicting the behavior of composite materials and enhance design parameters (Mansour et al. 2024b; Zhang et al. 2023). ML methods, such as artificial neural networks (ANNs) and support vector machines (SVMs), have shown exceptional performance in predicting the critical structural responses of FRP-confined concrete columns, such as load-bearing capacity, failure modes, and stress–strain response (Zhang et al. 2023). On the other hand, the hybridization of ML methods and numerical solutions for the assessment of the response of CFAT columns confined by AFRP is a new road of research. If successfully validated, this novel approach will pave the way for improved predictive modeling that can further advance the way structural design and assessment are performed.

Parallel to these developments, ML has emerged as a transformative tool in the field of structural engineering for predicting and optimizing the behavior of advanced composite systems. Talpur et al. (2024) employed a machine learning approach to predict the strength of concrete confined with sustainable natural FRP composites, demonstrating that ML can accurately capture nonlinear relationships between material properties and structural performance. Their findings highlight the capability of ML algorithms such as artificial neural networks (ANN) and support vector machines (SVM) in modeling complex composite behaviors that are difficult to capture using traditional analytical methods. In line with this trend, several recent studies have shown that integrating ML with experimental and numerical data significantly improves the accuracy and efficiency of predicting key performance indicators in FRP-confined concrete systems. Building upon this growing body of knowledge, the present study combines FEA and ML techniques to investigate the behavior of AFRP-confined CFAT columns, addressing the gap in existing literature and contributing toward the development of reliable, data-driven predictive models for sustainable composite structures.

Despite the progress in research on CFST, the literature on CFAT—particularly when strengthened with AFRP—remains very limited. Most previous studies have focused on CFAT columns' axial and cyclic behavior without external strengthening, while FRP-confinement research has concentrated mainly on CFRP and GFRP composites rather than AFRP. This has left a significant knowledge gap regarding the interaction mechanism between AFRP wrapping, aluminum tubes, and concrete cores under compression. Furthermore, existing confinement design models are largely empirical and based on steel tubes; due to the fundamental differences in material properties between aluminum and steel, these models may not reliably predict the confinement behavior or load-carrying capacity of CFAT columns. Additionally, there are conflicting findings in the literature concerning the influence of parameters such as the diameter-to-thickness ratio (D/t), concrete strength, and number of FRP layers on the overall performance and ductility of confined columns. Some studies report increased confinement efficiency with higher concrete strength or additional FRP layers, while others note diminishing returns or premature local buckling effects.

To bridge these inconsistencies, the present study integrates FEA and ML techniques to comprehensively assess AFRP-confined CFAT columns. The work specifically investigates how AFRP layers, tube geometry, and concrete strength interact to influence axial performance, aiming to provide reliable data and predictive models that can clarify these previously conflicting outcomes and support the development of more accurate design recommendations for AFRP-strengthened CFAT columns.

1.1 Research significance

This research is significant because novel strengthening techniques to improve CFAT Columns structural performance using advanced computational modeling will be proposed. This work comes to fill a gap in current knowledge on the behavior of aluminum-based composite structures by synthetically studying the implementation of AFRP confinement. The results are anticipated to provide support for the design of optimized strengthening methodologies that increase the load-bearing capacity, ductility, and energy dissipating capacity of CFAT columns, ultimately prolonging the service life of CFAT columns in engineering applications.

Moreover, the combination of ML with finite element analysis is an innovative contribution to the field of structural engineering, providing a new and efficient approach

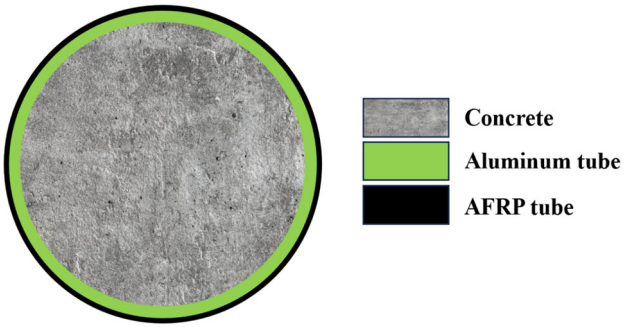


Fig. 1 Simulated CFAT AFRP-confined columns

to predicting the behavior of the AFRP-consolidating CFAT columns. Such a methodological leap can have more general implications in composite structural design and evaluation, paving the way for more efficient oversights and making it less dependent on often expensive in-built laboratory testing and cumbersome experimental works. This knowledge provides a solid foundation for the design of comprehensive global strengthening systems, and is essential to promote the theoretical and practical implementation of the integrated concept in structural applications, thus potentially addressing safety and sustainability of infrastructure systems. The simulated CFAT columns confined with AFRP wraps are shown in Fig. 1.

2 Experimental database

In structural engineering, CFAT columns have received interest for their light weight, resistance to corrosion, and aesthetics. The use of AFRP sheets as a means of confinement has proven to increase the axial loading capacity, ductility, and energy dissipation of columns. Reference was made to experimental data on 23 concrete-filled aluminum circular hollow section (CHS) stub columns tested by Zhou and Young (2009) to validate the FEA developed for this study. Uniform axial compression was applied to these specimens, and their structural performance was assessed based on the axial load-strain relationships, failure modes, and ultimate load capacities. The experimental data obtained through these tests were then utilized to validate the FEA to be integrated in the ABAQUS software (2017).

To add to the investigation, a parametric study was performed by simulating more specimens, varying the key design parameters: the number of AFRP layers, the concrete compressive strength, and the dimensions of the aluminum tube. Simulated specimens were created using both experimental and numerical data (113 specimens all up). This complete data table was subjected to GPU-based ML analysis. The dataset consists of: compressive strength of the concrete in (MPa), the diameter of the aluminum tube (mm), the thickness of the aluminum tube (mm), the number of AFRP layers, column length (mm) and ultimate axial load capacity in (kN). Information pertaining to 113 experimental and simulated specimens are detailed in Annexure I.

This comprehensive experimental and numerical dataset thus constitutes a solid basis to study the structural performance of AFRP-confined CFAT columns under axial loading and to develop predictive models based on machine learning methods. Proposed design recommendations, combined with supplementary findings, form a basis for minimizing critical vulnerabilities and maximizing structural resilience through the application of AFRP-strengthened CFAT columns, while the incorporation of experimental data through numerical simulations bolsters confidence in study outcomes and facilitates their future application in structural engineering practice. The methodology flowchart is illustrated in Fig. 2.

3 Finite element analysis (FEA)

The axial performance of CFAT circular columns confined with AFRP sheets was simulated with the application of the FEA. The FEA was modeled using ABAQUS software (2017), with the input of the material properties for concrete, aluminum and AFRP. In order to realistically reflect CFAT columns behavior, five components must be accurately modeled: the confined concrete, the circular aluminum tube, the circular AFRP tube, the interface between the concrete core and the aluminum tube, and the interface between the aluminum and AFRP tubes. Moreover, the type of element chosen and the mesh size are important in obtaining accurate results with a reasonable computational time when simulating structures that include interface elements.

3.1 Materials

In structural applications involving CFAT columns externally strengthened with AFRP sheets, the confinement provided by the aluminum tube and AFRP sheets significantly enhances the core concrete's strength and ductility. Accurate modeling of this confinement effect is crucial for predicting the behavior of such composite columns under axial loading. The confinement alters the stress–strain relationship of concrete, producing higher strength and more ductile behavior compared to unconfined concrete.

3.1.1 Concrete

Since aluminum and AFRP have unique mechanical properties, the confinement behavior of concrete in AFRP externally wrapped CFAT columns is fundamentally different when compared to typical concrete-filled steel tube systems. Two main elements play a part in the confinement mechanism,

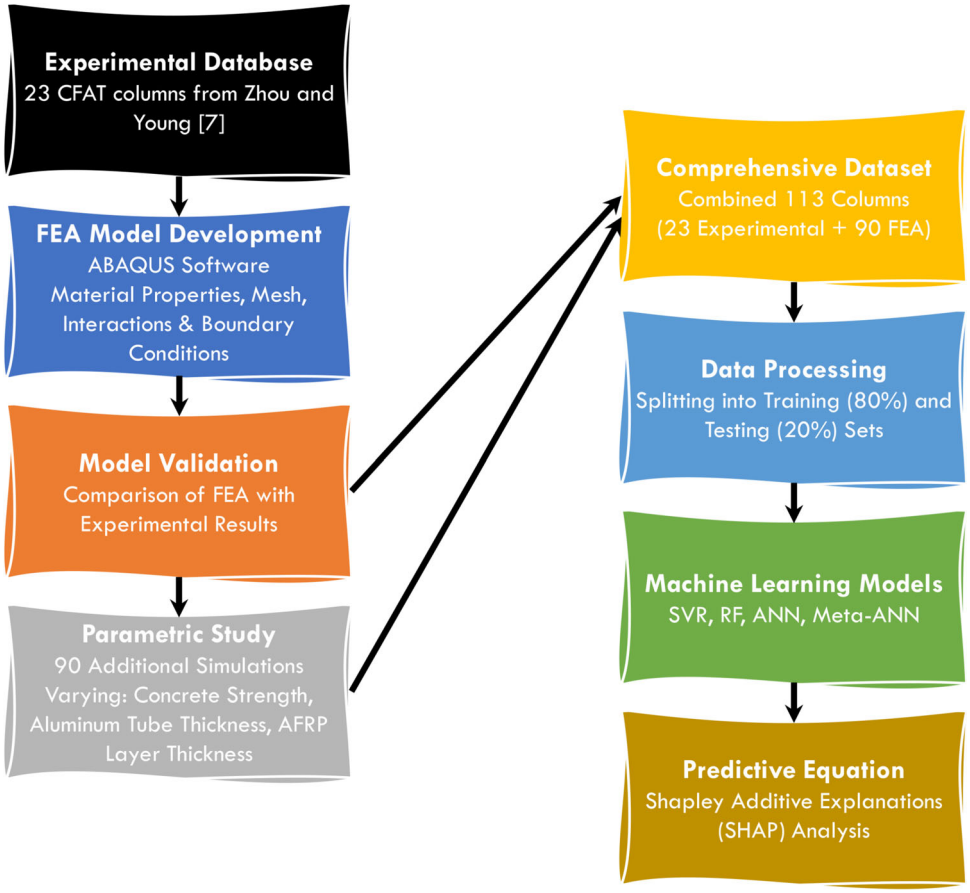


Fig. 2 Methodology utilized in the current study

namely the provision of initial lateral support usually performed by the aluminum tube and secondary reinforcement provided by the AFRP sheets aimed to increase the ultimate capacity and delay buckling. The uniaxial compressive strength with an associated strain for the laterally confined concrete presents a considerable increase when compared with their unconfined concrete. As shown in the uniaxial stress–strain diagram (Fig. 3) of concrete, unconfined concrete shows a completely different behavior from that of confined concrete, in which f_c, ε_c and f_{cc}, ε_{cc} indicate the compressive strength and corresponding strain of unconfined concrete and confined concrete, respectively. The stress–strain diagram for unconfined concrete is followed a typical pattern; the curve progresses in a linear elastic region to the peak stress, then it drops steeply because of brittle failure. On the contrary, the stress–strain behavior of confined concrete exhibits a gradual change from the elastic region to a greater peak stress followed by a larger softening branch indicating better ductility. The aluminum tube combined with AFRP sheets not only delays the peak failure but also reduces the strength degradation rate in the post-peak region due to confinement.

Three portions of the diagram need to be determined to define the complete equivalent uniaxial stress–strain curve

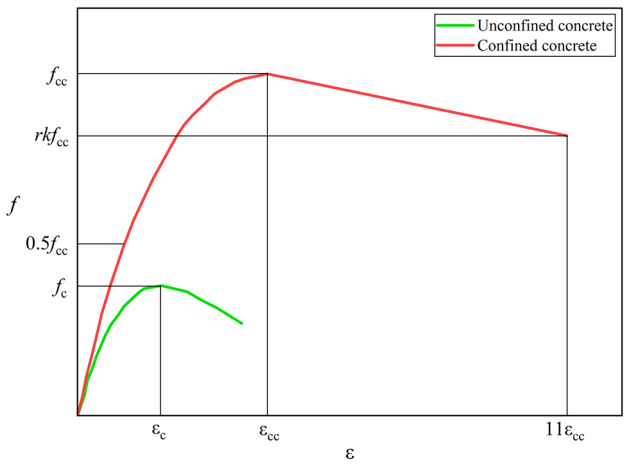


Fig. 3 Concrete's equivalent uniaxial stress–strain curve (Zhou and Young 2012)

for confined concrete. The first section is from the initially assumed elastic range up to the proportional limit stress. In this first region, confined concrete behaves similarly to unconfined concrete. As given by Hu et al. (2002), the value of the proportional limit stress is taken as ($0.5\,f_{cc}$). The elastic model of the constitutive equivalent of the confined concrete

is composed of its elastic modulus (E_{cc}) and Poisson's ratio (ν). The E_{cc} was calculated using Eq. 1 following the suggestion of ACI 318M-19 (Building Code Requirements for Structural Concrete and Commentary 2019), while for ν, it was assumed to be equal to 0.20 (Tao et al. 2013).

$$E_{cc} = 4700\sqrt{f_{cc}} \tag{1}$$

where f_{cc} represents the confined concrete compressive strength (measured in MPa). Equations 2 and 3, formulated by Mander et al. (1988), are used to calculate (f_{cc}) and its corresponding confined strain (ε_{cc}), respectively.

$$f_{cc} = f_c + k_1 f_l \tag{2}$$

$$\varepsilon_{cc} = \varepsilon_c\left(1 + k_2\frac{f_l}{f_c}\right) \tag{3}$$

where f_l represents the lateral confining pressure exerted by the AFRP sheets and aluminum tube. This pressure (f_l) is influenced by the D/t ratio (diameter-to-thickness ratio), the yield stresses (f_y) of the aluminum tube and AFRP sheets, and the unconfined concrete's compressive strength (f_c). Equation 4, introduced by Tao et al. (2013), calculates the lateral confining stress acting on the core concrete. The coefficients (k_1) and (k_2), set to 4.1 and 20.5 respectively, are based on the work of Richart et al. (1928). Using these values of (f_l), (k_1) and (k_2), the equivalent uniaxial confined concrete strength (f_{cc}) and its corresponding confined strain (ε_{cc}) can be computed through Eqs. 2 and 3.

$$f_l = \frac{(1 + 0.027 f_y)e^{-0.02\frac{D}{t}}}{1 + 1.6e^{-10(f_c)^{4.8}}} \tag{4}$$

When the load is increased, the concrete passes into the second region, when whose strength significantly grows because of lateral confinement pressure presented by the aluminum tube and AFRP wraps. This segment of the curve represents the nonlinear behavior starting at the proportional limit stress ($0.5 f_{cc}$) and extending to the confined concrete strength (f_{cc}). Equation 5, developed by Desayi and Krishnan (1964), models this portion of the curve. This equation relates multidimensional stress and strain values to their equivalent uniaxial counterparts. The unknowns in the equation are the uniaxial stress (f) and strain (ε) that characterize this region. Strain values (ε) are defined within the proportional strain range (calculated as $0.5\frac{f_{cc}}{\varepsilon_{cc}}$) and the confined strain (ε_{cc}), which corresponds to the confined strength (f_{cc}). By inputting assumed strain values (ε) into Eq. 5, the corresponding stress values (f) can be derived.

$$f = \frac{E_{cc}\varepsilon}{1 + (R + R_E - 2)\left(\frac{\varepsilon}{\varepsilon_{cc}}\right) - (2R - 1)\left(\frac{\varepsilon}{\varepsilon_{cc}}\right)^2 + R\left(\frac{\varepsilon}{\varepsilon_{cc}}\right)^3} \tag{5}$$

where R_E and R values are calculated from Eqs. 6 and 7, respectively.

$$R_E = \frac{E_{cc}\varepsilon_{cc}}{f_{cc}} \tag{6}$$

$$R = \frac{R_E(R_\sigma - 1)}{(R_\varepsilon - 1)^2} - \frac{1}{R_\varepsilon} \tag{7}$$

After reaching the peak stress, the concrete enters into the descending part (third part) where the load-carrying capacity of the concrete gradually decreases. The data in the form of softening behavior is modeled theoretically based on the exponential decay equation that resemble the gradual disappearance of strength as illustrated in the Eq. 8. The post-peak response of concrete is more stable with the inclusion of AFRP sheets compared with confined concrete where post-peak does not exist after the peak stress is reached. The AFRP wrapping anchors ensuring delayed outward local buckling of the aluminum tube under compression, thus, enhancing the ultimate load capacity of the systems and increasing overall structural performance.

$$f = rkf_{cc} + (f_{cc} - rkf_{cc})\left\{\frac{\varepsilon_c - 0.02}{\varepsilon_{cc} - 0.02}\right\},\ \varepsilon_{cc} \le \varepsilon_c \le 11\varepsilon_{cc} \tag{8}$$

where rk is the strength degradation parameter proposed by Hu et al. (2003) as shown in Eq. 9.

$$= \begin{cases} 1.0,\ 22 \le D/t \le 40 \\ 1.3491 + 0.000339\left(\frac{D}{t}\right)^2 - 0.010085\left(\frac{D}{t}\right),\ 40 \le D/t \le 150 \end{cases} \tag{9}$$

To validate the selection of the coefficients k_1, k_2, and r_k used in the confinement model, a sensitivity analysis was conducted to evaluate their influence on the predicted confined concrete strength and strain. Each coefficient was varied systematically by ± 10–20% within its calibrated range while keeping other parameters constant. The results demonstrated that k_1, which governs confinement efficiency, and k_2, which controls strain enhancement, have the most pronounced impact on the axial load capacity predictions. In contrast, changes in r_k, which defines post-peak strength degradation, had a comparatively minor effect, indicating its stability.

The concrete core in the AFRP-confined CFAT columns is primarily subjected to triaxial compressive stress, the

expansion of compressive failure surface with increasing hydrostatic pressure is the main factor affecting concrete failure. Therefore, linear Drucker-Prager yield criterion was utilized in this study with the associate flow and isotropic hardening rule. According to Zhou and Young (2012), the material angle of friction (β_{cc}) and the ratio of flow stress in triaxial tension to that in compression (k) were set at 20^0 and 0.8, respectively.

Hence, even if CFAT columns confined with AFRP wraps are less sensitive to the tensile properties of the concrete under axial compression, tension stiffening has to be defined in the ABAQUS. For the current model, the uniaxial tensile response was assumed to be linear till the tensile strength of concrete, taken as $0.1 f_c$, was reached. Fracture energy (G_f) was employed to characterize the tensile softening behavior beyond this failure stress. Therefore, the fracture energy (G_f) and tensile strength (f_t) of the confined concrete were modeled with Eq. 10 (Tang et al. 2020) and Eq. 11 (Building Code Requirements for Structural Concrete and Commentary 2019) as follows.

$$G_f = 2.5\left(10^{-3}\right)\alpha(0.1 f_{cc})^{0.7} \tag{10}$$

$$f_t = 0.33\sqrt{f_{cc}} \tag{11}$$

where $\alpha = 1.25 d_{max} + 10$ and d_{max} is the coarse aggregate diameter in the concrete in (mm).

3.1.2 Aluminum

Due to the absence of an obvious yield step in the stress- strain response of aluminum tube, its constitutive curve is different from ordinary carbon steel. Drawing on earlier research, Chen et al. (2022) employed the constitutive model for the aluminum tube simulating the confining marine concrete columns. Moreover, Wang et al. (2023) successfully used this model for round-ended CFT columns where CFRP tube is wrapped around an aluminum tube and got good agreement with the test results. This is the Ramberg–Osgood (Amir et al. 2022) model that has successfully been used to simulate aluminum compressive response. This model is able to accurately characterize the varying nonlinear characteristics of aluminum alloy and steel. The constitutive model can be expressed by Eq. 12 as follows:

$$\varepsilon = \begin{cases} \frac{f}{E_0} + 0.002\left(\frac{f}{f_{0.2}}\right)^n & f < f_{0.2} \\ \frac{(f - f_{0.2})}{E_{0.2}} + \left\{\frac{0.008 - (f_{1.0} - f_{0.2})}{E_{0.2}\frac{(f - f_{0.2})}{(f_{1.0} - f_{0.2})}}\right\}^{n\prime_{0.2,1.0}} & f \geq f_{0.2} \end{cases} \tag{12}$$

where the strain (ε) and stress (f) of aluminum are taken into account. The 0.2% proof stress ($f_{0.2}$) and 1% proof stress ($f_{1.0}$) are also considered. Moreover, the strain at $f_{0.2}$ ($\varepsilon_{0.2}$) and the modulus of elasticity of the aluminum tube (E_0) are taken into account. The stiffness at $f_{0.2}$ is expressed as $E_{0.2}$. The values for $n\prime_{0.2,1.0}$ can be obtained from a previous study performed by Wang et al. (2019). Additionally, the Poisson's ratio of aluminum tube is taken as 0.33 (Zhou and Young 2012).

3.1.3 AFRP

AFRP is a type of composite consisting of aramid fibers parallel to each other and oriented in one direction. It can be regarded as an anisotropic material, with high tensile strength along the fiber direction, while the strength perpendicular to the fiber direction is negligible. The properties of AFRP sheets in ABAQUS are defined as an "Engineering Constants" material type, and parameters are similar with Ref. (Djerrad et al. 2024) as shown in Table 1.

3.2 Element types and meshes

In terms of meshing strategy, a structured hexahedral mesh (C3D8R elements) was used for both the concrete and aluminum tube from the ABAQUS (2017) software's element library, ensuring high accuracy and computational efficiency. A mesh convergence study was conducted by varying the global element size, and the mesh with an element size of approximately 5 mm in the radial direction was selected as the optimal configuration to balance accuracy and computational cost. The AFRP wrapping was modeled using shell elements (S4R) with an equivalent thickness representing the total number of layers. The refined mesh near the tube ends captured local stress concentrations and confinement effects.

3.3 Interactions, loading, and boundary conditions

The interaction modeling begins with the contact between the aluminum tube and the concrete core, which was defined using a *surface-to-surface contact* formulation. In this setup, the inner surface of the aluminum tube was designated as the slave surface, while the outer surface of the concrete core acted as the master surface (Ding et al. 2021; Zhou and Young 2012). The contact included both *normal* and *tangential* behaviors—normal behavior was modeled using the "hard contact" formulation to allow separation after compression, while tangential behavior was defined through a penalty friction model with a friction coefficient of 0.25, as supported by previous studies. This ensured realistic load transfer and confinement effects between the two materials.

For the AFRP–aluminum interface, a perfect bonding assumption was applied since the aramid fiber wrap was externally adhered using epoxy. This was implemented using the "tie constraint" function in ABAQUS (2017), which

Table 1 Characteristics of AFRP wraps (Djerrad et al. 2024)

Elasticity parameters (MPa)			Poisson's ratio			Shear modulus parameters (MPa)		
E_1	E_2	E_3	μ_{12}	μ_{13}	μ_{23}	G_{12}	G_{13}	G_{23}
79,000	5500	5500	0.36	0.36	0.36	2300	2300	2000

prevents any relative slip between the AFRP layer and the aluminum tube. In this constraint, the AFRP wrap was defined as the *master surface* and the aluminum tube as the *slave surface*, ensuring continuous stress transfer across the interface.

The loading and boundary conditions were established to replicate the experimental test setup accurately. The bottom end of the CFAT column was fully fixed in all translational and rotational degrees of freedom through a reference point (RP-2), while the top end (RP-1) was constrained against rotation and lateral movement but allowed vertical displacement to simulate axial compression. The loading was applied under displacement control, where a uniform vertical displacement was imposed on the top surface nodes to ensure an even stress distribution across the column cross-section. The top and bottom surfaces were coupled kinematically to maintain uniform deformation and prevent stress localization.

3.4 Dataset generation and parametric analysis

After validating the finite element (FE) model against 23 experimental results from previous studies, a comprehensive parametric study was performed in ABAQUS to generate an additional 90 simulated cases, bringing the total dataset to 113 data points. The objective of this numerical program was to systematically evaluate the influence of key design variables—tube geometry, AFRP confinement ratio, and concrete strength—on the axial load-carrying behavior of AFRP-confined CFAT columns.

The main parameters varied in the simulation include column diameter (150 mm and 300 mm), aluminum tube thickness (2, 4, and 8 mm), AFRP layers (0, 1, 3, 5, and 7 layers), and unconfined concrete compressive strength ($f'c$) (30, 50, and 70 MPa). These combinations resulted in $2 \times 3 \times 5 \times 3 = 90$ unique configurations. The chosen ranges were selected to represent realistic design conditions found in lightweight structural applications. The diameters were chosen to reflect both slender and compact column geometries, while the tube thicknesses correspond to D/t ratios ranging from 18.75 to 75, capturing the transition from thin-walled, buckling-prone sections to thick, confinement-dominant ones. The AFRP layer counts represent common strengthening levels used in practical retrofitting applications, allowing assessment of confinement efficiency and the potential for diminishing strength gains beyond five layers. The selected concrete strengths span from normal to high strength to explore the combined effects of confinement and material stiffness.

Each simulation adopted the same boundary conditions, material models, and contact interactions as described in Sects. 3.2 and 3.3 to ensure that performance variations were solely attributed to the selected parameters. The column height was fixed at 500 mm, resulting in L/D ratios of 3.33 and 1.67 for the 150 mm and 300 mm diameter columns, respectively, to examine the influence of slenderness. The generated dataset provided a comprehensive matrix of results capturing the complex interplay between AFRP confinement level, aluminum tube geometry, and core strength. These results were later used to develop and train ML models, enabling accurate prediction and feature-importance analysis of the axial behavior of AFRP-confined CFAT columns. The complete details of all 113 simulated configurations are provided in Appendix (Table 5) for reference and reproducibility (Fig. 4).

4 Results and discussion

4.1 Comparison of experimental and FEA results

A total of 23 concrete-filled aluminum circular hollow section (CHS) stub columns that experimentally tested by Zhou and Young (2009) were used to verify the validity of FEA used in the current study. The axial load-strain relationships and ultimate load capacities of these specimens were evaluated under uniformly distributed axial compression. The experimental data were compared to FEA predictions (in ABAQUS (2017) software) which are summarized in Table 2. As demonstrated in Fig. 5, axial load-strain curves from experimental tests and FEA simulations were highly comparable for most specimens. For example, the specimens with lower concrete strength ($f_c = 40-70$ MPa) and smaller D/t ratios (e.g., CHS1C40, CHS2C40) exhibited nearly overlapping curves, suggesting that the FEA covered the elastic and post-peak behavior of confined concrete quite well. For each curve, a bilinear response was usually observed: A linear elastic branch and a nonlinear ascending branch resulted from the combined confining action of the aluminum tube. Table 2 lists the ultimate axial loads obtained from the experimental results and those predicted by the FEA. The range of the P_{EXP}/P_{FEA} ratio was 0.85–1.14, with an average of

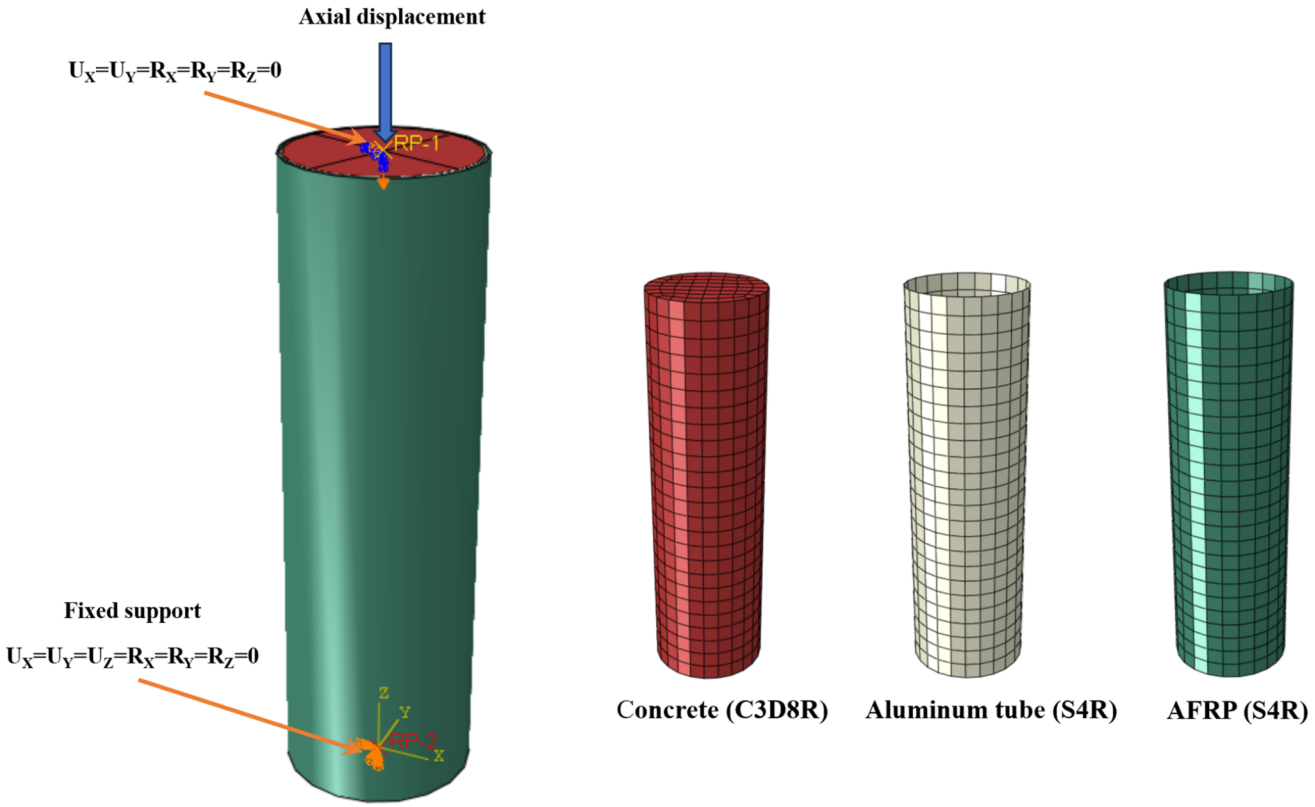


Fig. 4 Element types, mesh size, and boundary condition of the FEA model

0.98 and a standard deviation of 0.09, indicating a good overall agreement between these two measurements. The model demonstrates robust performance in predicting confinement effects even in high-strength infill specimen (e.g., CHS3C100: 1.00; CHS6C100: 1.01) with higher concrete strength ($f_c = 100$ MPa) corresponding to lower P_{EXP}/P_{FEA} ratio.

The axial stress–strain curves of all the experimental and simulated CFAT columns (Fig. 5) under compression can be described by a common trend which consists of four well-defined stages. Since the columns are in a linear elastic stage at first, deformation is controlled by the composite stiffness of the concrete core and aluminum tube which has not yet been confined by AFRP wrapping. With the increase of loading, the response shifts to a nonlinear ascending stage characterized by microcracking and decreasing stiffness in which the aluminum tube restrains lateral dilation and confining action of AFRP confinement becomes apparent as it further mobilizes stress redistribution. This is followed by the peak load stage, where the axial stress reaches its maximum value (f_{cc}) at a strain ε_{cc}; AFRP-wrapped specimens such as CHS7C100 achieve significantly higher peak stresses and strains than unconfined columns due to synergistic confinement and delayed local buckling. Finally, in the post-peak stage a fast drop in stress (for unconfined specimens) or an extended plateau followed by gradual softening (for AFRP-confined columns such as CHS5C70 and CHS7C40) is observed where effective confinement prohibits radial expansion of the column and induces ductility until failure through progressive crushing, tube buckling or rupture of the AFRPs. This entire stress–strain path highlights the significant contribution of AFRP confinement in enhancing strength, displacement ductility and energy dissipation at all loading stages.

4.2 Effects of test variables

In order to further improve the comprehensiveness of the numerical study, the finite element modeling modelling was extended to examine 90 more specimens, for a total of 113, with the systematic variation of critical parameters, including AFRP layers, concrete compressive strength, aluminum tube thickness, column diameter, and column height. The details of all 113 specimens are provided in Appendix (Table 5).

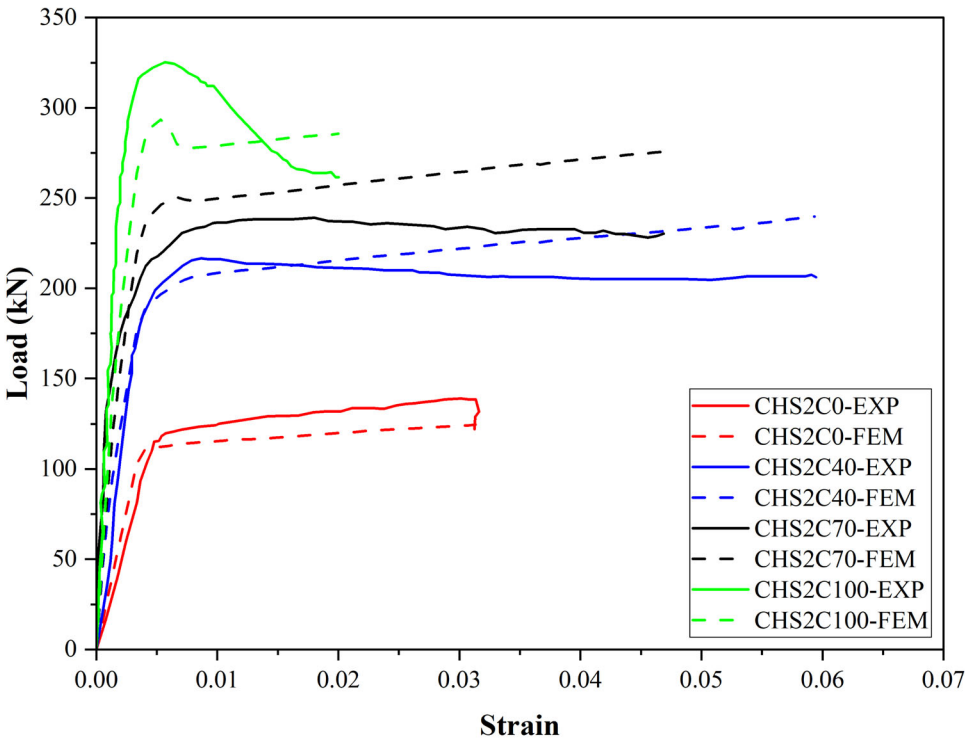
4.2.1 Effect of concrete strength

Figures 6, 7 and 8 illustrates the influence of unconfined concrete compressive strength f_c on the ultimate axial load capacity of AFRP-confined CFAT columns with a diameter

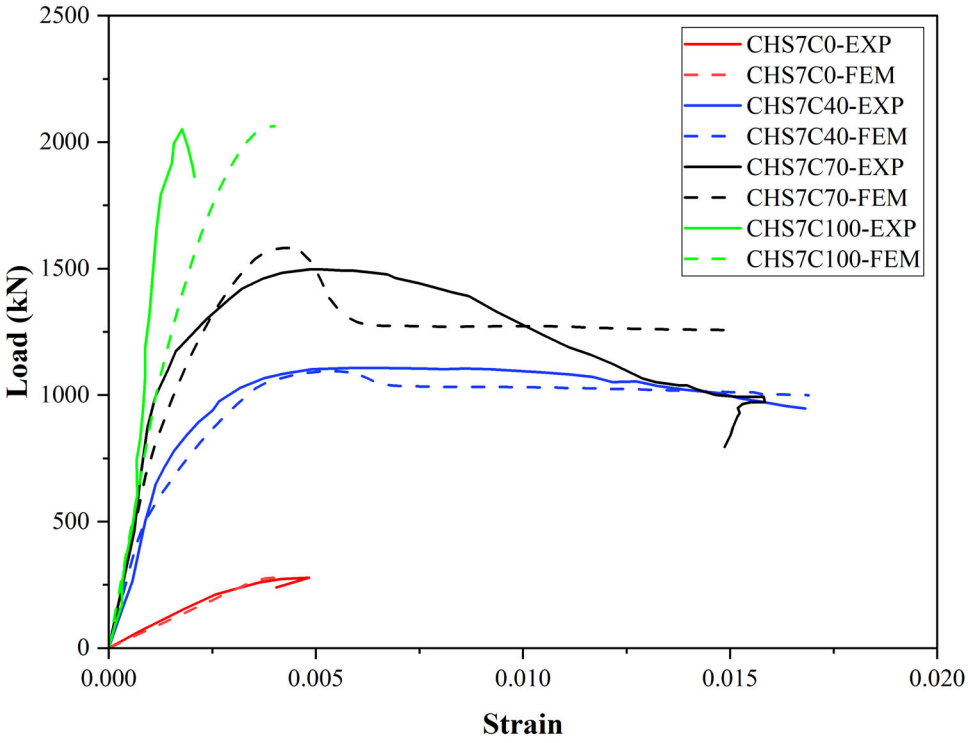
Table 2 Comparison between experimental and numerical CFAT AFRP-confined columns

ID	Peak strength of unconfined concrete, f_c (MPa)	Geometrical properties						Ultimate load, P_{EXP} (kN)	Ultimate load, P_{FEA} (kN)	P_{EXP}/P_{FEA}
		Diameter of column, D (mm)	Height of column, H (mm)	Thickness of aluminum tube, t_{al} (mm)	Diameter of concrete infill, D_c (mm)	D/t	H/D			
CHS1C40	40	38	114	3.89	30.22	9.77	3	158.9	163	0.97
CHS1C70	70	38	114	3.9	30.2	9.74	3	167.2	186	0.90
CHS1C100	100	38	114	3.92	30.16	9.69	3	171.5	201	0.85
CHS2C0	0	50	150	3.13	43.74	15.97	3	141.2	125	1.13
CHS2C40	40	50	150	3.13	43.74	15.97	3	217	229	0.95
CHS2C70	70	50	150	3.12	43.76	16.03	3	238.9	275	0.87
CHS2C100	100	50	150	3.13	43.74	15.97	3	327.5	293	1.12
CHS3C40	40	60	180	2.55	54.9	23.53	3	244.1	276	0.88
CHS3C70	70	60	180	2.54	54.92	23.62	3	292.4	344	0.85
CHS3C100	100	59.9	180	2.53	54.84	23.68	3	412.6	411	1.00
CHS4C40	40	76.1	228	2.06	71.98	36.94	3	329.9	351	0.94
CHS4C70	70	76	228	2.06	71.88	36.89	3	415.7	457	0.91
CHS4C100	100	76	228	2.05	71.9	37.07	3	611.4	574	1.07
CHS5C40	40	99.7	300	2.02	95.66	49.36	3	543.6	517	1.05
CHS5C70	70	99.8	300	2.06	95.68	48.45	3	712	727	0.98
CHS5C100	100	100	300	2.05	95.9	48.78	3	995.8	937	1.06
CHS6C40	40	119.8	360	2.49	114.82	48.11	3	822.8	757	1.09
CHS6C70	70	120	360	2.55	114.9	47.06	3	1010.3	1065	0.95
CHS6C100	100	119.9	360	2.48	114.94	48.35	3	1388.7	1369	1.01
CHS7C0	0	149.8	449	2.51	144.78	59.68	3	283.9	281	1.01
CHS7C40	40	150.1	450	2.53	145.04	59.33	3	1111.1	1095	1.01
CHS7C70	70	150.1	451	2.54	145.02	59.09	3	1496.4	1582	0.95
CHS7C100	100	149.9	450	2.53	144.84	59.25	3	2057.8	1813	1.14

of 150 mm, varying aluminum tube thicknesses (yielding D/t ratios of 18.75, 37.5, and 75), and AFRP layers (0, 1, 3, 5, 7). The results reveal that increasing f_c consistently enhances the ultimate load capacity across all D/t ratios, though the magnitude of improvement depends on the interplay between concrete strength, aluminum tube confinement, and AFRP reinforcement. For columns with thicker aluminum tubes (D/t = 18.75, Fig. 6), the inherent confinement from the aluminum tube dominates, resulting in higher baseline load capacities even without AFRP. Here, the addition of AFRP layers provides incremental gains, particularly at higher f_c values, as the combined confinement from aluminum and AFRP optimizes stress redistribution, delaying buckling and enhancing ductility. In contrast, columns with thinner aluminum tubes (D/t = 75, Fig. 8) exhibit a stronger reliance on AFRP confinement. The absence of AFRP leads to significantly lower capacities, but increasing the number of layers substantially amplifies load-bearing performance, especially for high-strength concrete, where AFRP effectively compensates for the aluminum tube's reduced stiffness. For intermediate D/t ratios (37.5, Fig. 7), the synergy between aluminum and AFRP confinement is more balanced, with AFRP layers progressively mitigating the limitations of moderate aluminum thickness. Across all cases, higher f_c amplifies the efficacy of AFRP, as stiffer concrete core interacts more effectively with the confinement mechanisms. These findings underscore that the enhancement in load capacity due to concrete strength is non-linear and highly contingent on the composite action between aluminum, AFRP, and concrete, with thicker aluminum tubes offering inherent robustness, while thinner tubes necessitate strategic AFRP reinforcement to achieve comparable performance.



(a) CHS2C0 to CHS2C100 specimens



(b) CHS7CO to CHS7C100 specimens

Fig. 5 Comparison between experimental and FEA results from Zhou and Young (2009)

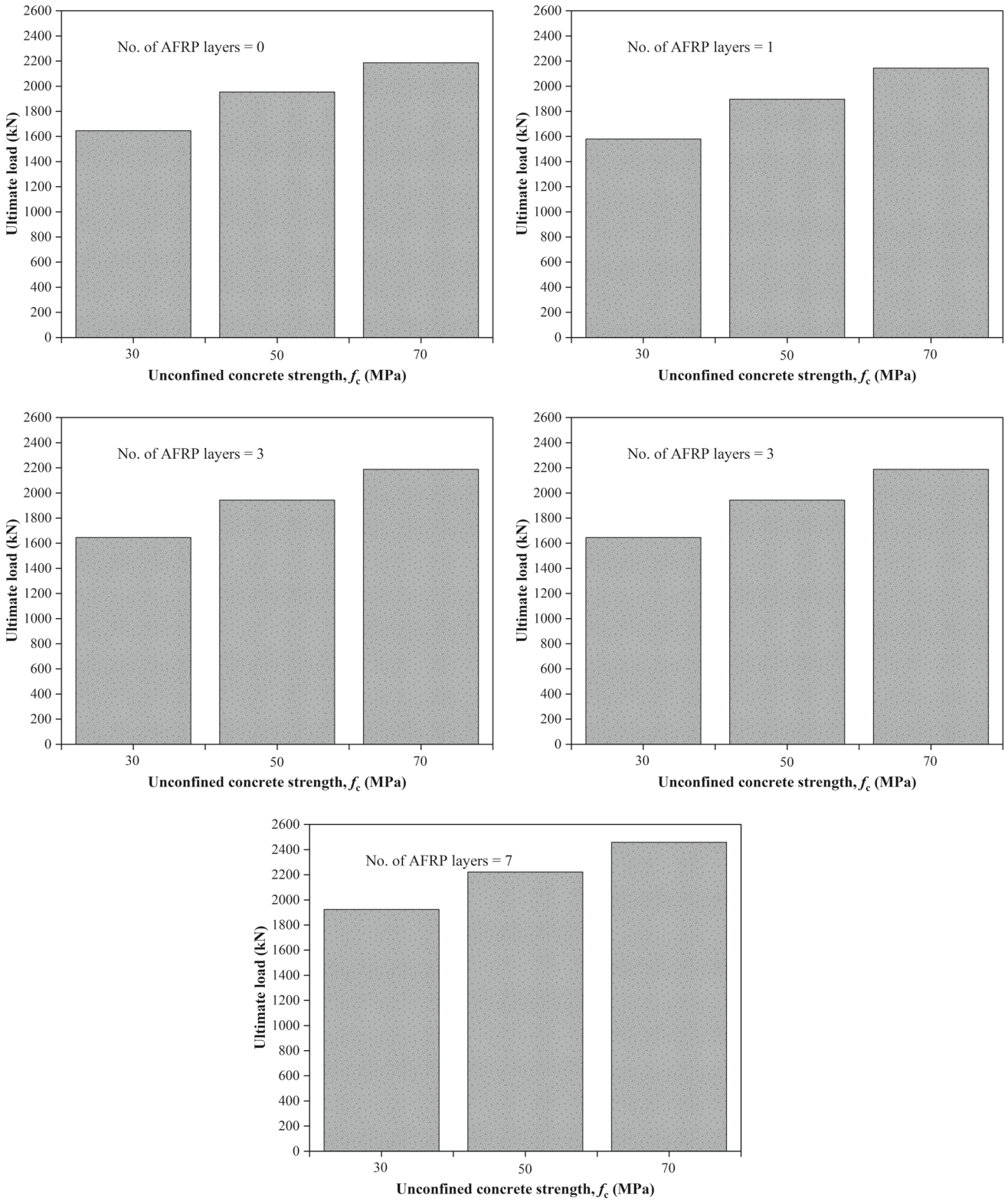


Fig. 6 Ultimate load versus peak strength of unconfined concrete for columns having D/t = 18.75 with varying AFRP layers

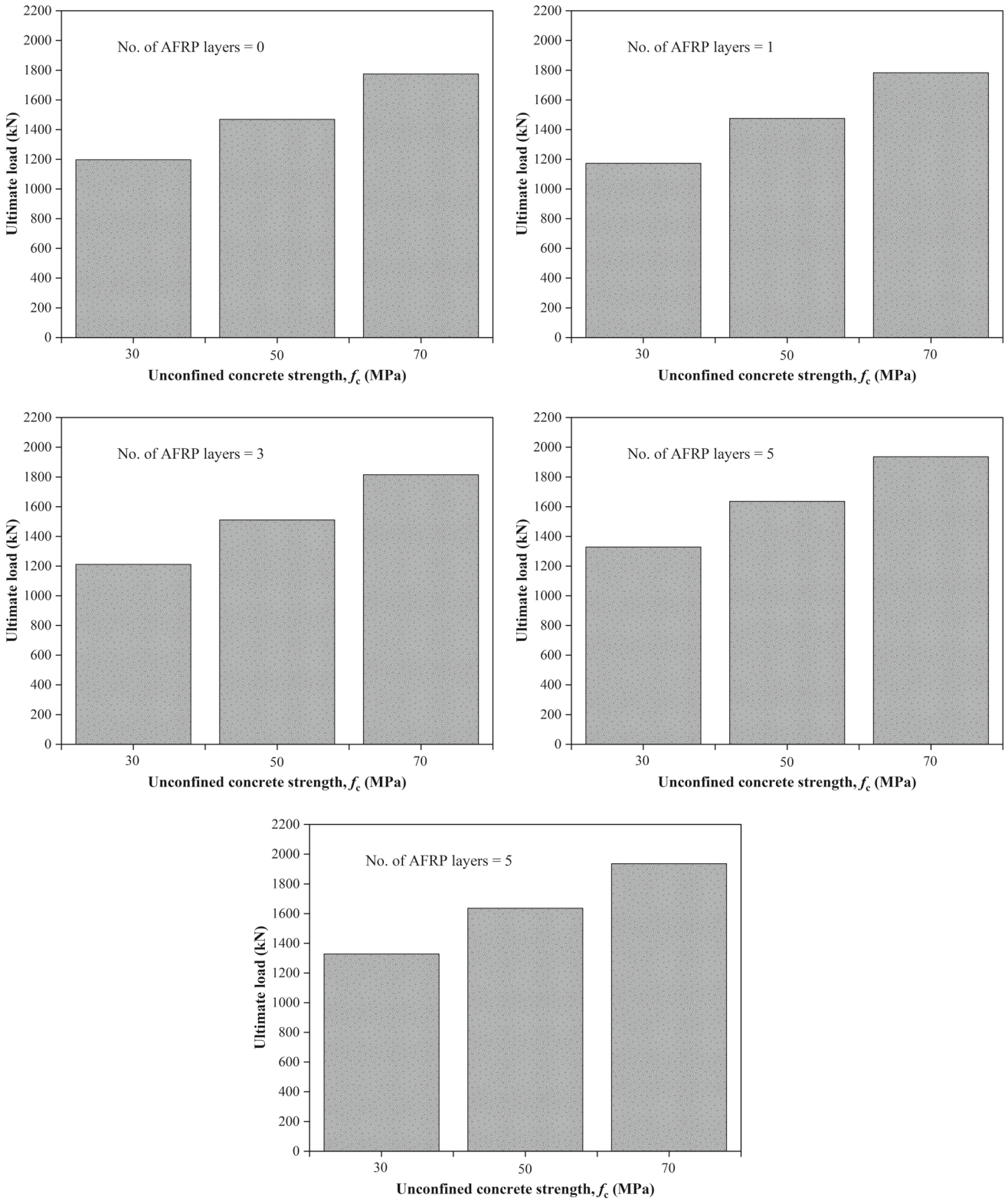


Fig. 7 Ultimate load versus peak strength of unconfined concrete for columns having D/t = 37.5 with varying AFRP layers

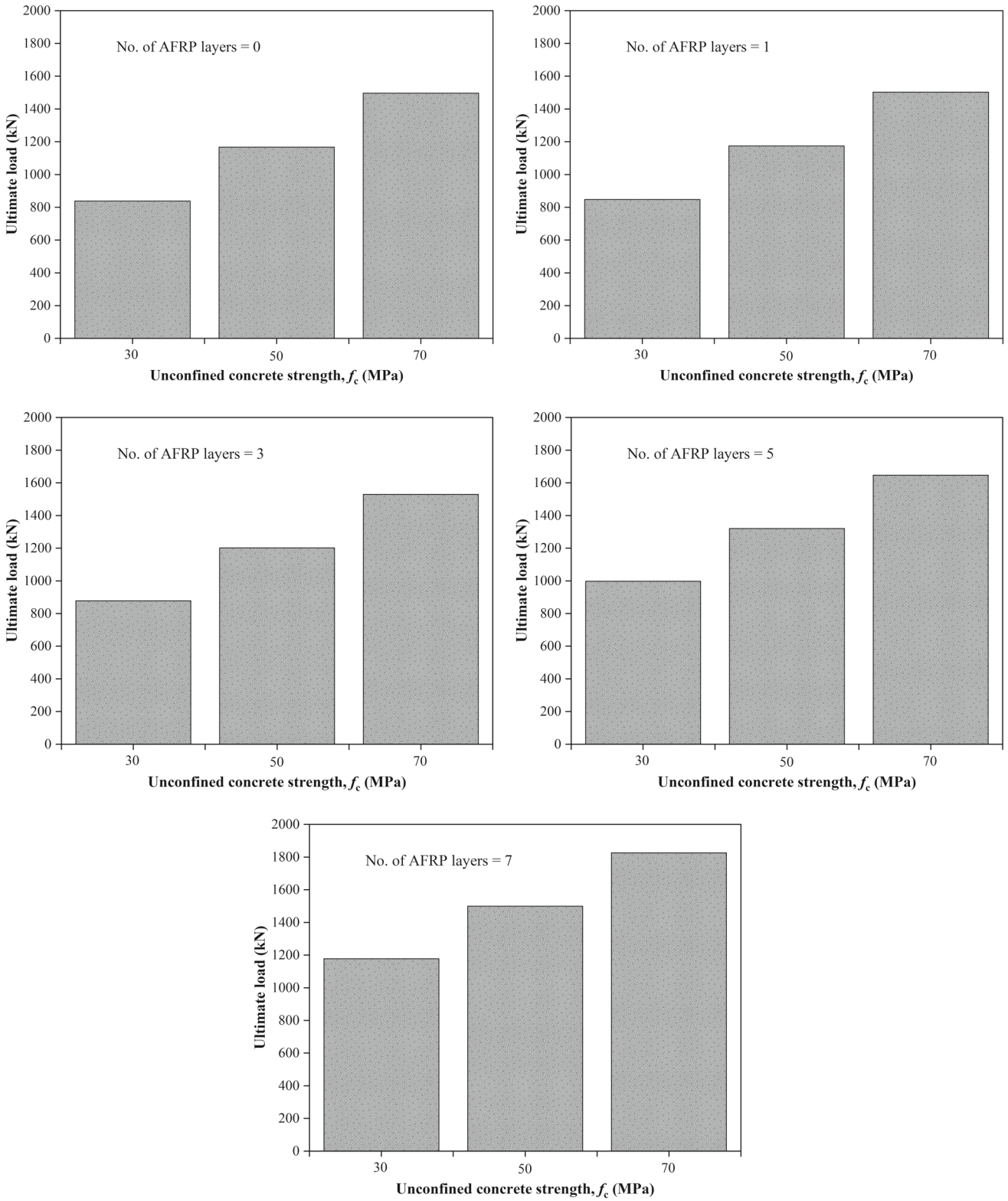


Fig. 8 Ultimate load versus peak strength of unconfined concrete for columns having D/t = 75 with varying AFRP layers

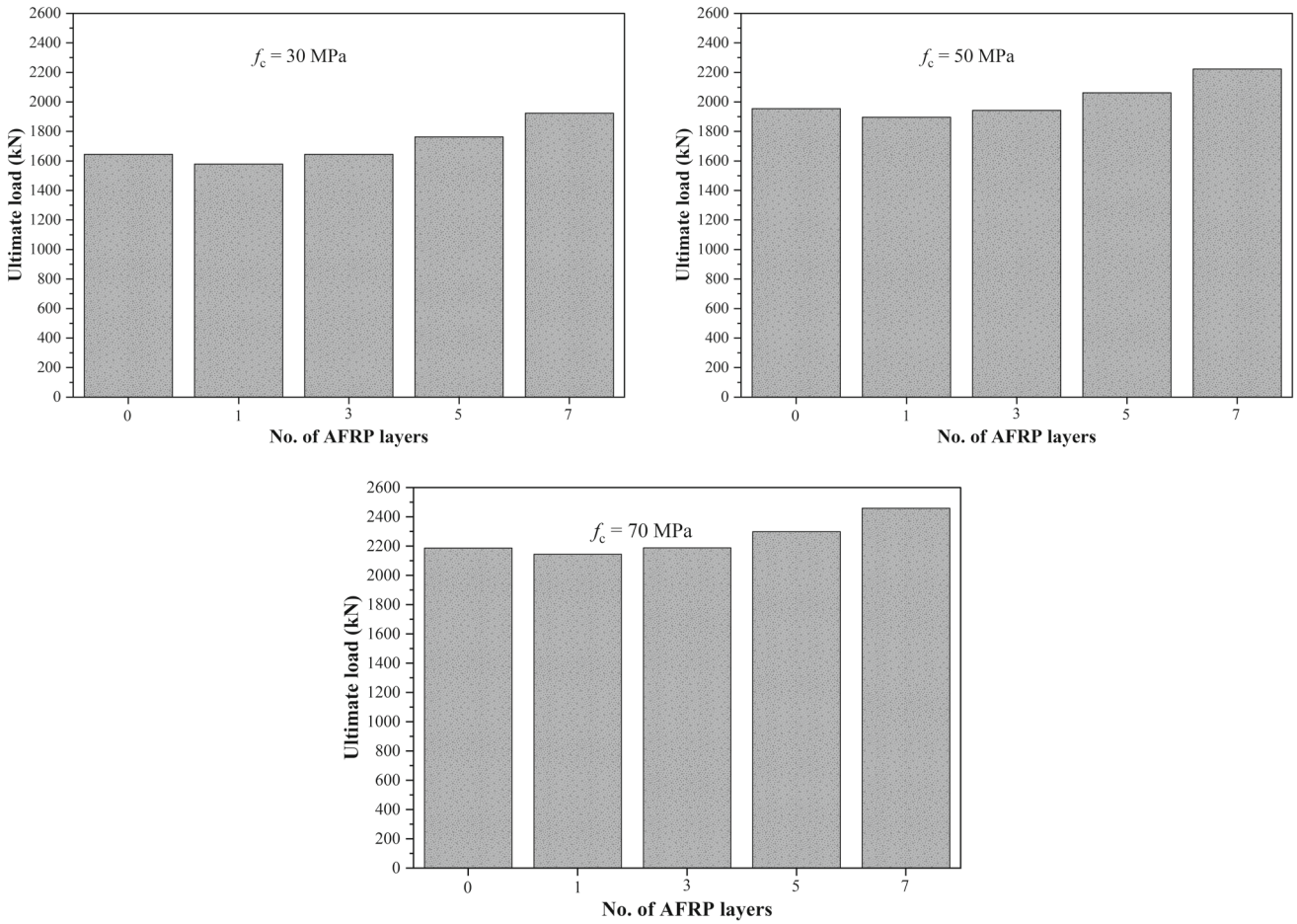


Fig. 9 Ultimate load versus peak strength of unconfined concrete for columns having D/t = 18.75 with varying unconfined concrete strengths

4.2.2 Effect of AFRP layers

Figures 9, 10 and 11 illustrate the influence of AFRP layer quantity on the ultimate axial load capacity of CFAT columns with a fixed diameter of 150 mm, varying aluminum tube thicknesses (2, 4, 8 mm), corresponding to D/t ratios of (75, 37.5, 18.75), and unconfined concrete strengths (f_c= 30, 50, 70 MPa). The findings reveal that increasing AFRP layers consistently enhances load capacity across all D/t ratios, though the magnitude of improvement depends on the interplay between aluminum confinement efficacy and concrete strength. For columns with thin aluminum tubes (D/t = 75, t = 2 mm), AFRP layers significantly compensate for the aluminum's limited stiffness, yielding substantial load gains. For instance, at f_c= 70 MPa (Fig. 11), increasing AFRP layers from 0 to 7 raises the ultimate load by almost 22%, as AFRP mitigates buckling and amplifies confinement. Conversely, thicker aluminum tubes (D/t = 18.75, t = 8 mm) exhibit inherent robustness, where AFRP provides incremental benefits (e.g., almost17% increase at f_c = 70 MPa) due to the dominant confinement from the aluminum. Intermediate D/t ratios (37.5, t = 4 mm) show balanced synergy, with AFRP layers progressively enhancing capacity by up to almost 19% at higher f_c. Notably, higher f_c amplifies AFRP's efficacy: for D/t = 75, the load improvement from 0 to 7 AFRP layers rises from around 40% (f_c = 30 MPa) to around 22% (f_c = 70 MPa), reflecting diminishing returns as concrete strength dominates. The nonlinear relationship between AFRP layers and load capacity underscores that initial layers (1–3) provide the most significant gains, with diminishing enhancements at higher layer counts. These trends highlight that AFRP reinforcement is most critical for slender aluminum tubes (high D/t), where confinement is weak, while thicker tubes (low D/t) benefit less but still achieve measurable improvements. The results emphasize the necessity of optimizing AFRP usage based on aluminum thickness and concrete strength to maximize cost-efficiency and structural performance.

In order to illustrate more clearly the effect of AFRP confining for structural behavior, percentages of ultimate axial load capacity increases in comparison with unconfined CFAT columns are summarized in Table A-1, for different configurations. The findings are evident that significant strengths are due to AFRP confinement, notably in samples with thin aluminum tubes (high D/t ratios); being the efficiency of

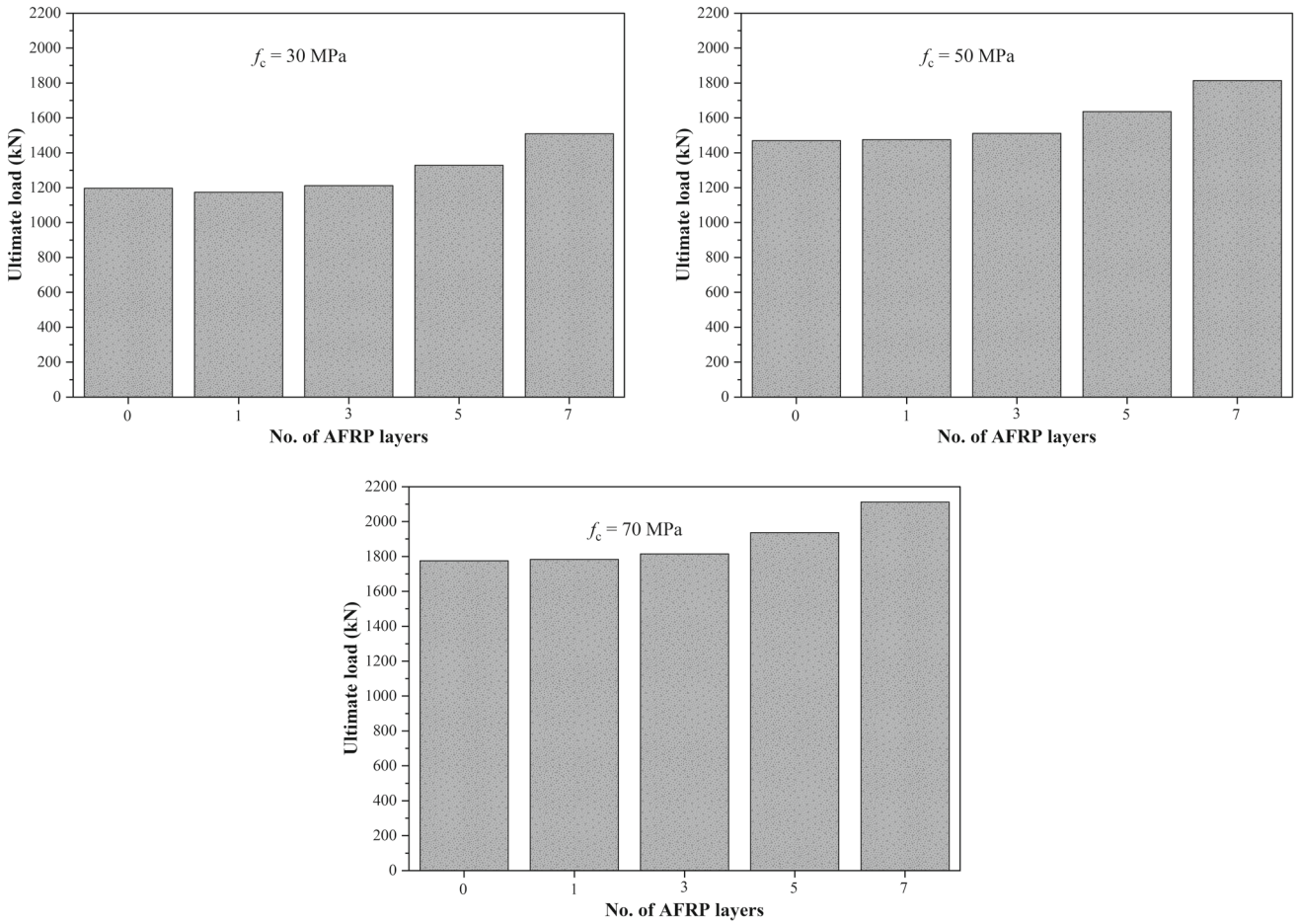


Fig. 10 Ultimate load versus peak strength of unconfined concrete for columns having D/t = 37.5 with varying unconfined concrete strengths

confining low for those without exterior reinforcement. The specimens with less initial confinements and more layers of AFRP received the most significant improvements, demonstrating that using AFRP could be a valuable option of increasing the load capacity.

The results clearly demonstrate that the structural performance of AFRP-confined CFAT columns is governed by a strong interaction among the aluminum tube D/t ratio, the number of AFRP layers, and the concrete strength. Columns with higher D/t ratios benefit more significantly from AFRP confinement due to their inherently lower initial confinement, leading to more pronounced strength gains with each added layer. Conversely, specimens with lower D/t ratios show reduced incremental improvements, indicating that the aluminum tube alone provides substantial confinement. Furthermore, increasing concrete strength enhances the overall load-bearing capacity; however, the relative benefit of AFRP confinement tends to decrease as the concrete matrix itself becomes more dominant. These findings highlight the synergistic nature of composite action, where the simultaneous optimization of tube geometry, AFRP reinforcement, and concrete strength is essential for achieving maximum structural efficiency.

4.3 Effect of investigated parameters on mechanical performance

To provide a deeper understanding of how key parameters influence the structural response of AFRP-confined CFAT columns, a comprehensive analysis was conducted to evaluate their effects on ultimate stress capacity, dilation behavior, and ductility. Table 3 summarizes the results of five selected specimens, including the percentage changes relative to the reference (unconfined) specimens.

The results indicate that increasing the number of AFRP layers consistently enhances the ultimate stress capacity due to improved confinement, with the most pronounced effects observed in columns with higher D/t ratios where the aluminum tube alone provides limited confinement. Conversely, columns with lower D/t ratios exhibited more moderate improvements, highlighting the combined role of tube stiffness and external wrapping.

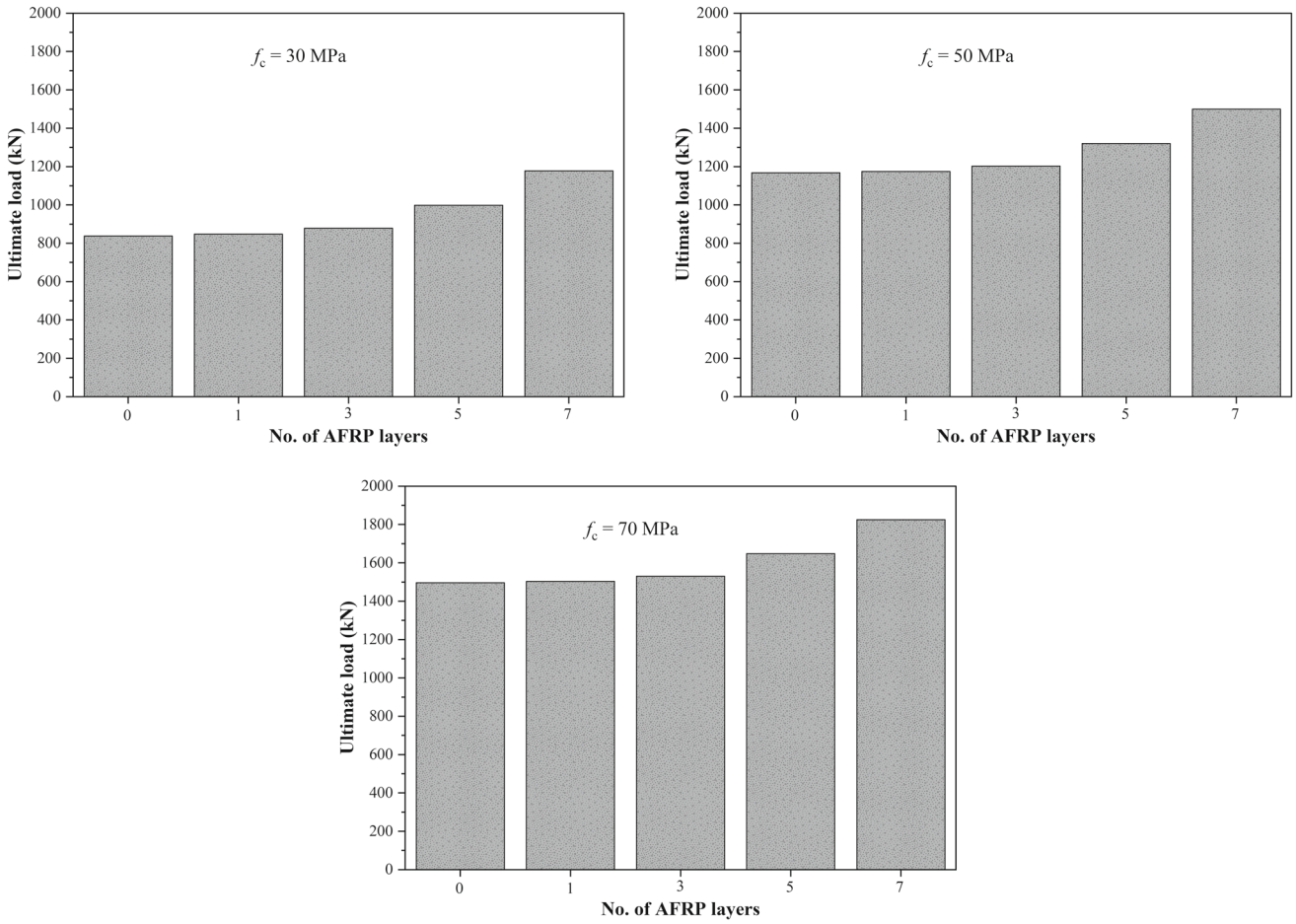


Fig. 11 Ultimate load versus peak strength of unconfined concrete for columns having D/t = 75 with varying unconfined concrete strengths

Table 3 Effect of investigated parameters on ultimate stress capacity, dilation properties, and column ductility

Specimen ID	D/t ratio	Concrete strength (MPa)	AFRP layers	Ultimate load (kN)	% Change vs. unconfined	Dilation strain ($\times 10^{-3}$)	% Change vs. unconfined	Ductility index	% Change vs. unconfined
S1 (Ref.)	75	30	0	838.29	–	3.25	–	2.15	–
S2	75	30	5	997.88	+ 19.05%	2.76	− 15.08%	2.78	+ 29.30%
S3	75	30	7	1177.84	+ 40.53%	2.51	− 22.77%	3.46	+ 60.93%
S4	37.5	30	7	1509.03	+ 26.11%	2.63	− 19.08%	3.32	+ 54.42%
S5	18.75	70	7	2458.68	+ 12.45%	2.48	− 23.69%	3.89	+ 80.93%

Dilation behavior exhibited a decreasing trend with increased AFRP layers, indicating more effective confinement and delayed volumetric expansion. This reduction in lateral deformation also contributed to improved ductility, as reflected by the ductility index, which showed significant enhancement in all confined specimens. The synergy between the three parameters confirms the importance of optimizing composite action to achieve superior structural performance.

5 ML modeling

5.1 Methods and evaluation

In this paper, four ML models were developed and evaluated to predict the CFAT strength based on inputs generated using finite element analysis (see Sect. 2). These models include Support Vector Regression (SVR), Random Forest (RF), Artificial Neural Network (ANN), and Metaheuristic-Optimized ANN (Meta-ANN). The data was divided into

training (80%) and testing (20%) subsets, and all input features were normalized using z-score normalization which defines as $X_{norm} = \frac{X-\mu X}{\sigma X}$, where, μ is the mean of the variable and σ is the standard deviation.

The selection of the four machine learning models—SVR, RF, ANN, and Meta-ANN—was guided by their complementary capabilities in modeling nonlinear structural behavior and achieving balanced accuracy–interpretability performance. The Support Vector Regression (SVR) model was employed for its robustness with small datasets and its ability to capture nonlinear relationships through kernel functions, minimizing overfitting risks. The Random Forest (RF) algorithm was chosen due to its ensemble-based architecture, which effectively handles complex variable interactions and provides feature-importance insights, facilitating interpretation of key parameters such as AFRP layers, *D/t* ratio, and concrete strength. The Artificial Neural Network (ANN) was adopted for its flexibility in learning intricate nonlinear relationships among geometric and material parameters influencing axial strength. To further enhance predictive performance, a Meta-ANN model was developed by integrating multiple optimized ANN architectures, improving generalization and reducing model bias. While SVR and RF offer greater stability and interpretability, ANN and Meta-ANN deliver superior accuracy for highly nonlinear behaviors. This combination of models ensures a comprehensive and comparative framework for evaluating predictive performance in AFRP-confined CFAT columns.

In this study, z-score normalization was selected as the data preprocessing method to standardize input features before training the machine learning models. Unlike min—max scaling, which compresses data within a fixed range (typically 0 to 1) and can be sensitive to outliers, z-score normalization transforms features based on their mean and standard deviation. This approach ensures that all variables are centered around zero with a standard deviation of one, thereby maintaining their relative distributions and reducing the dominance of features with larger numerical ranges. Moreover, since our dataset contains variables with different units and scales, z-score normalization provides a more balanced representation, which helps improve model convergence and predictive performance.

The SVR model is developed using a radial basis function (RBF) kernel. Its hyperparameters, i.e., box constraint, kernel scale, and epsilon margin, are optimized via Bayesian Optimization. Similarly, the RF regression model, built using the bagging ensemble method, has its primary hyperparameter (number of learning cycles) optimized through the same approach. A feedforward ANN model with a single hidden layer is also developed, where Bayesian Optimization determined the optimal number of neurons (1–30). The network is trained using the Levenberg–Marquardt algorithm with ReLU activation in the hidden layer. The Meta-ANN is developed to explore deeper architectures in an ANN. Genetic Algorithm (GA) optimizes both the number of hidden layers, between 1 and 3, and the neurons per layer, between 0 and 30, running for 100 generations with a population size of 30. This methodology has been used in different fields. Interested readers in details of this methodology are referred to Kandiri et al. (2024); Kandiri et al. 2022). All Bayesian Optimization procedures were conducted with a maximum of 100 objective evaluations. To assess the accuracy of each model, the root mean square error (RMSE), mean absolute error (MAE), mean absolute percentage error (MAPE), and Pearson's correlation coefficient (R) are utilized.

$$R = \frac{\sum_{j=1}^{T}(E_j - \overline{E})(A_j - \overline{A})}{\sum_{j=1}^{T}(E_j - \overline{E})^2 \sum_{j=1}^{T}(A_j - \overline{A})^2} \tag{13}$$

$$RMSE = \sqrt{\frac{1}{T}\sum_{j=1}^{T}(A_j - E_j)^2} \tag{14}$$

$$MAE = \frac{1}{T}\sum_{j=1}^{T}|A_j - E_j| \tag{15}$$

$$MAPE = \frac{100}{T}\sum_{j=1}^{T}\left|\frac{A_j - E_j}{A_j}\right| \tag{16}$$

where E_j, $\overline{E}$, A_j, $\overline{A}$, T, are the estimated output, average of estimated outputs, actual values of the output, average of actual output, the number of data records in the dataset, respectively.

5.2 Model performance comparison

Table 4 summarizes the evaluation metrics for all models, while Fig. 12 shows a cross-validation comparing models' performances.

5.3 Explanatory results

Predicted ultimate strength of CFAT columns can serve as a valuable indicator for analyzing the performance of CFAT. For such practical applications, it is crucial that the underlying predictive models remain understandable, allowing practitioners to gain a deeper understanding of the impact and importance of each component. This methodology is especially useful for pinpointing which factors play the largest roles when predicted strength deviates significantly from normal trends. To support this analysis, this study employs the Shapley Additive Explanations (SHAP) framework (Lundberg and Lee 2017). SHAP is based on cooperative game theory and is used to interpret machine learning predictions by calculating Shapley values. These values help explain how and why a model's prediction differs from the average and

Table 4 The error indicators comparing the models' performances

Model	RMSE		MAE		MAPE		R	
	Train	Test	Train	Test	Train	Test	Train	Test
SVR	43.24	61.93	34.2	49.77	2.29	3.49	0.99	0.99
RF	36.81	51.78	29.87	42.59	2.12	3.48	0.99	0.99
ANN	102.37	132.05	75.68	97.74	4.57	5.92	0.99	0.99
Meta-ANN	48.14	67.02	24.54	29.88	1.67	2.02	0.99	0.99

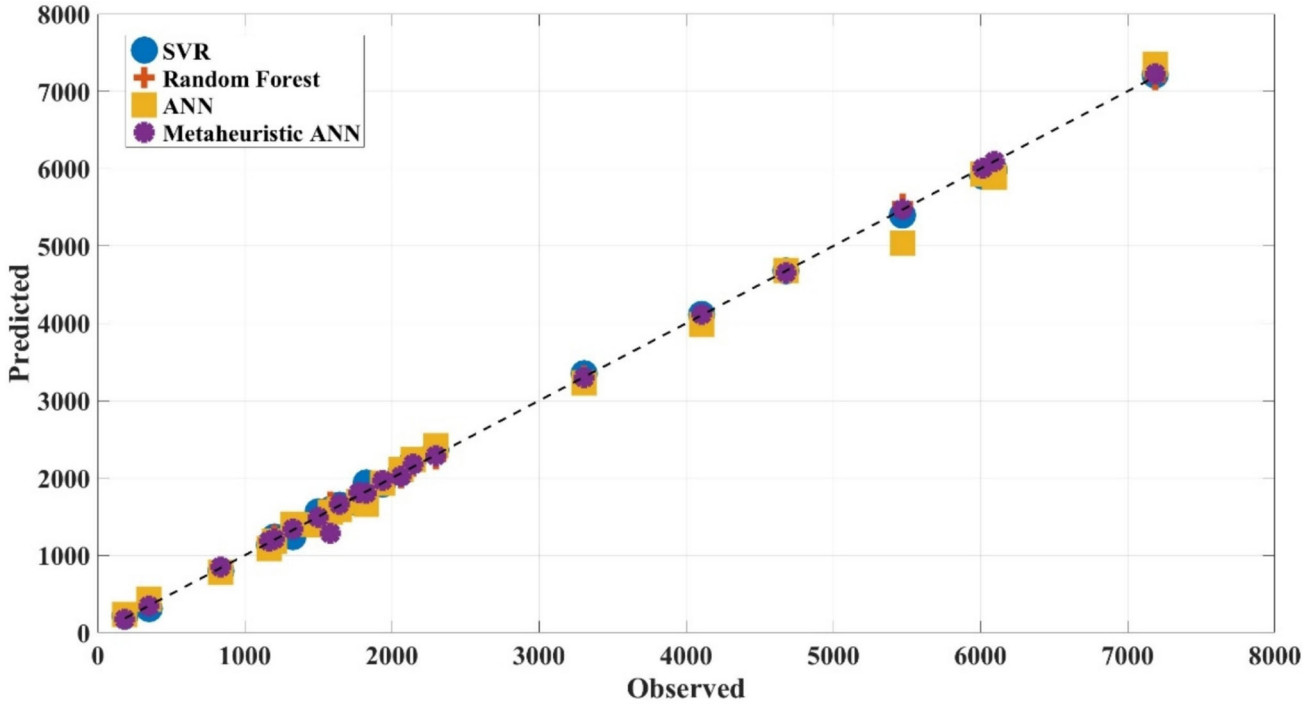


Fig. 12 Cross-validation comparison of predicted versus observed ultimate strength (kN) using four different machine learning models

quantify each input feature's influence on the result. A Shapley value represents a feature's average contribution across all possible combinations of inputs (Molnar 2020). For each subset of features, the marginal contribution of including a specific variable is determined by comparing the outcome with and without that variable.

In essence, the SHAP value captures how much a specific feature shifts the prediction away from the baseline average. For every individual data point, the total departure from the mean output is the sum of the SHAP values for all features involved. The SHAP value for feature a and the query point q is calculated as follows:

$$\varphi_a(v_q) = \frac{1}{B} \sum_{S \subseteq \beta\{a\}} \frac{v_q(S \cup \{a\}) - v_q(S)}{\frac{(B-1)!}{|S|!(B-|S|-1)!}} \tag{17}$$

where B represents the total number of features, v_q is the predicted value for input point q, β denotes the full feature set, and $|S|$ is the size of subset S. Figure 13 shows the SHAP figures.

The interpretability outcomes derived from the SHAP analysis are strongly consistent with both the earlier FEA results and the predictive trends observed in the ML models. For instance, SHAP identified the aluminum tube D/t ratio and the number of AFRP layers as the most influential parameters governing axial load capacity—a finding that mirrors the numerical simulations, where variations in these parameters significantly altered confinement behavior and load-bearing performance. Similarly, the importance of concrete strength in the SHAP results aligns with the experimental and FEA evidence that higher compressive strength enhances confinement efficiency but reduces the relative contribution of AFRP wrapping. This consistency between model interpretability, numerical simulations, and engineering intuition not only validates the robustness of the ML framework but also reinforces confidence in its predictive reliability for practical structural applications.

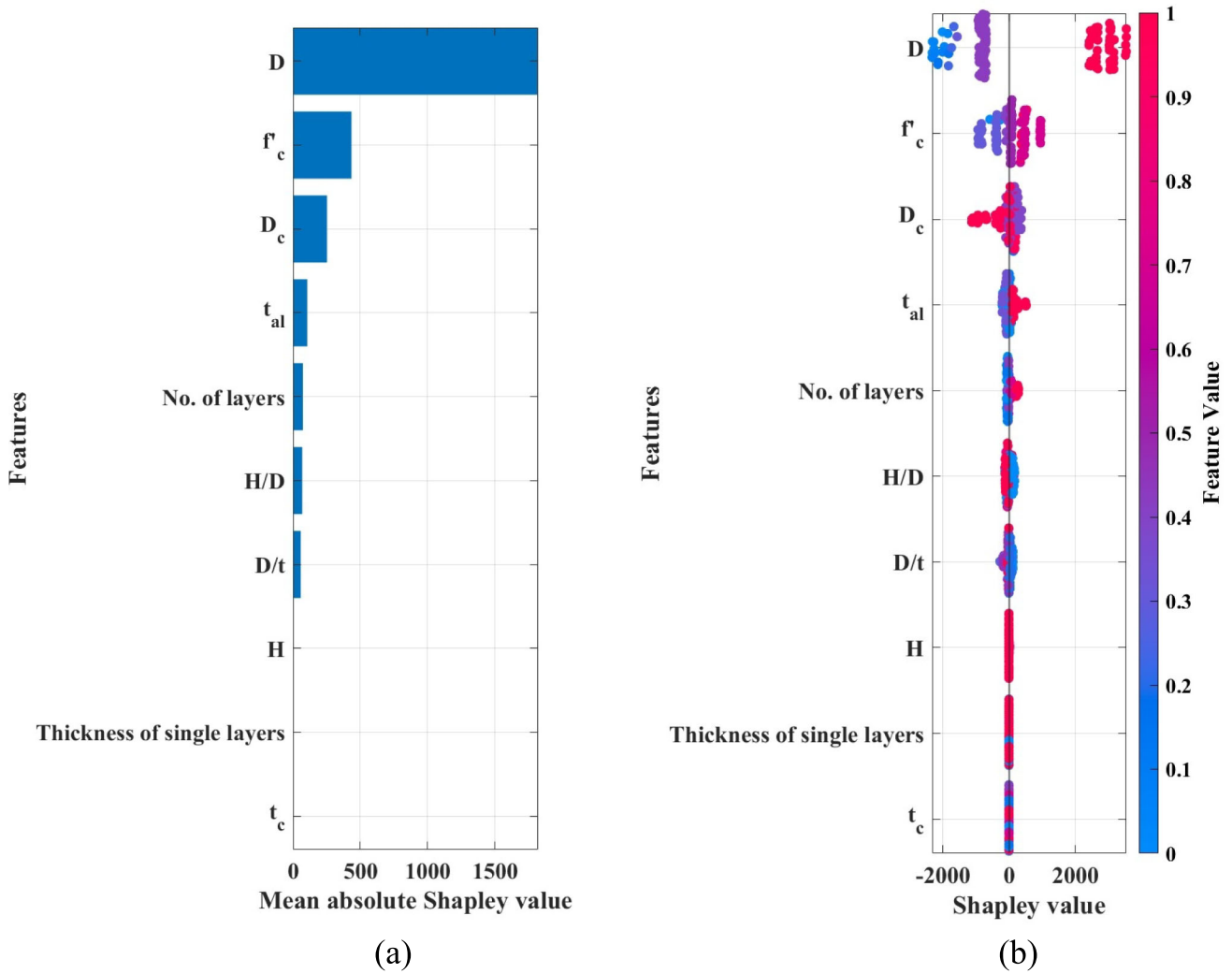


Fig. 13 SHAP values. **a** mean absolute Shapley value, **b** Shapley value

Figure 13a shows a horizontal bar chart summarizing the mean absolute SHAP values for each input variable. This reflects how much each feature, on average, contributes to the prediction across all samples. As can be seen, D is by far the most influential feature, followed by f'_c, D_c, and t_{al}. These findings align with engineering expectations, as the overall geometry and material strength directly affect the strength of CFAT. Other parameters like the number of layers, slenderness ratios (H/D, D/t), and individual layer thickness appear to have relatively minor influences.

Figure 13b is a bee swarm SHAP plot, which not only reaffirms feature importance but also illustrates how the value of each feature impacts predictions. Each point represents a prediction instance; the colour represents the original feature value (blue = low, red = high), and the position on the x-axis shows the SHAP value (i.e., the effect on model output). For the diameter (D), higher values (in red) consistently push predictions higher, indicating a strong positive correlation with ultimate strength. Similarly, higher values of f'_c and D_c are also associated with increased predicted CFAT strength. Interestingly, some features show mixed effects—for example, t_{al} displays both positive and negative contributions depending on its range, suggesting a more complex interaction with other variables.

To provide a broader context for the obtained results, the findings of this study were compared with recent investigations on fiber-reinforced composite strengthening of concrete members. Saingam et al. (2024) demonstrated that hemp FRP rope confinement in recycled aggregate concrete columns substantially enhanced both compressive strength and ductility, achieving up to 181% strength and 564% strain improvement compared with unconfined specimens. These gains were most significant in low-strength concrete, and the authors highlighted discrepancies between experimental and analytical predictions, supporting the need for refined or data-driven confinement models. Similarly, Rodsin et al. (2023)

reported that glass-FRP (GFRP) confinement of reinforced concrete beams produced considerable increases in load-carrying capacity, with the most notable gains (up to 72%) for anchored full and U-shaped wraps, effectively reducing brittle shear failures. Meanwhile, Joyklad et al. (2024) found that ferrocement and FRP composite strengthening of one-way reinforced concrete slabs significantly improved structural performance, increasing peak load by 49%, ultimate deflection by 109%, and energy dissipation by 174% compared with unstrengthened slabs.

6 Conclusions

This study presented a comprehensive investigation into the structural performance of AFRP-confined CFAT columns under axial loading through finite element analysis and predictive modeling. The following key conclusions can be drawn:

1- The finite element analysis model developed in ABAQUS accurately simulated the axial behavior of CFAT columns, showing strong agreement with experimental results from 23 tested specimens.
2- The ratio of experimental to numerical ultimate load capacity (PEXP/PFEA) ranged between 0.85 and 1.14, with an average value of 0.98 and a standard deviation of 0.09, confirming the model's reliability across varying parameters.
3- The inclusion of AFRP sheets significantly enhanced the axial capacity and ductility of CFAT columns, especially for columns with thin aluminum tubes (high D/t ratios) where the aluminum alone provides limited confinement.
4- The confinement effect was also reflected in the dilation behavior of the specimens. The presence of AFRP layers effectively restricted lateral expansion and improved the overall volumetric stability of the columns, contributing to a more controlled deformation response.
5- A substantial improvement in column ductility was observed with increased AFRP confinement, as indicated by higher ductility indices. This enhancement demonstrates the effectiveness of AFRP wrapping in delaying failure and extending the post-peak deformation capacity of the composite columns.
6- For specimens with D/t = 75, increasing AFRP layers from 0 to 7 resulted in up to 40% improvement in axial capacity. Even for thicker tubes (D/t = 18.75), enhancements up to 17% were observed, demonstrating the effectiveness of AFRP reinforcement across different tube thicknesses.
7- Higher unconfined concrete strength (f'c) led to a nonlinear increase in axial load capacity across all specimens. The confinement effectiveness of AFRP was more pronounced in specimens with higher concrete strengths, where the synergy between a stiffer core and external confinement yielded superior performance.
8- The combined influence of AFRP and concrete strength is critical in optimizing the ultimate load-bearing capacity of CFAT columns.
9- ML models successfully predicted the axial strength of AFRP-confined CFAT columns with high accuracy ($R \approx 0.99$). Among them, the Meta-ANN model achieved the lowest mean absolute percentage error (MAPE = 2.02%), proving its superior predictive capability.
10- SHAP analysis revealed that column diameter was the most influential parameter, followed by concrete compressive strength, concrete core diameter, and aluminum tube thickness. The findings provide critical insights for design optimization by identifying the most impactful variables on structural performance.
11- The incorporation of ML techniques represents a novel and efficient approach for structural performance prediction, reducing dependency on exhaustive experimental procedures.
12- The findings underscore the value of integrating AFRP confinement in CFAT columns for applications demanding high performance-to-weight ratios, such as in offshore structures, long-span bridges, and high-rise buildings.

Despite the promising findings of this study, several limitations should be acknowledged. First, the finite element models were validated using a limited set of experimental data primarily focused on stub columns under axial compression; as such, the results may not fully capture the behavior of slender columns or those subjected to combined loading conditions such as bending or torsion. Additionally, while the material models used for aluminum and AFRP were derived from established literature, actual material behavior may vary due to manufacturing inconsistencies or long-term environmental exposure. The ML models, though highly accurate, rely on the quality and scope of the dataset used for training and may have limited generalizability outside the tested parameter ranges. Therefore, future research should focus on expanding experimental validation to include slender columns, dynamic or cyclic loading conditions, and varying environmental exposures. Moreover, developing generalized design equations and refining ML models with larger, more diverse datasets could further improve the reliability and applicability of predictions in real-world structural applications.

Appendix

See Table 5.

Table 5 Experimental data (from literature) and simulation results (from parametric studies) for AFRP-confined CFAT columns

No	Peak strength of unconfined concrete, f_c (MPa)	AFRP properties			Geometrical properties						Experimental results	FEA results	% Increase vs unconfined
		No. of layers	Thickness of single layer (mm)	Total thickness, t_f (mm)	Diameter of column, D (mm)	Height of column, H (mm)	Thickness of aluminum tube, t_{al} (mm)	Diameter of concrete core, D_c (mm)	D/t	H/D	Ultimate load (kN)	Ultimate load (kN)	
1	40	–	–	–	38	114	3.89	30.22	9.77	3	159	163	–
2	70	–	–	–	38	114	3.9	30.2	9.74	3	167	186	–
3	100	–	–	–	38	114	3.92	30.16	9.69	3	172	201	–
4	0	–	–	–	50	150	3.13	43.74	15.97	3	141	125	–
5	40	–	–	–	50	150	3.13	43.74	15.97	3	217	229	–
6	70	–	–	–	50	150	3.12	43.76	16.03	3	239	275	–
7	100	–	–	–	50	150	3.13	43.74	15.97	3	328	293	–
8	40	–	–	–	60	180	2.55	54.9	23.53	3	244	276	–
9	70	–	–	–	60	180	2.54	54.92	23.62	3	292	344	–
10	100	–	–	–	59.9	180	2.53	54.84	23.68	3	413	411	–
11	40	–	–	–	76.1	228	2.06	71.98	36.94	3	330	351	–
12	70	–	–	–	76	228	2.06	71.88	36.89	3	416	457	–
13	100	–	–	–	76	228	2.05	71.9	37.07	3	611	574	–
14	40	–	–	–	99.7	300	2.02	95.66	49.36	3	544	517	–
14	70	–	–	–	99.8	300	2.06	95.68	48.45	3	712	727	–
16	100	–	–	–	100	300	2.05	95.9	48.78	3	996	937	–
17	40	–	–	–	119.8	360	2.49	114.82	48.11	3	823	757	–
18	70	–	–	–	120	360	2.55	114.9	47.06	3	1010	1065	–
19	100	–	–	–	119.9	360	2.48	114.94	48.35	3	1389	1369	–
20	0	–	–	–	149.8	449	2.51	144.78	59.68	3	284	281	–
21	40	–	–	–	150.1	450	2.53	145.04	59.33	3	1111	1095	–
22	70	–	–	–	150.1	451	2.54	145.02	59.09	3	1496	1582	–
23	100	–	–	–	149.9	450	2.53	144.84	59.25	3	2058	1813	–
24	30	0	0	0	150	500	2	146	75.00	3.33	–	838.29	–
25	30	1	0.2	0.2	150	500	2	146	75.00	3.33	–	847.93	1.15
26	30	3	0.2	0.6	150	500	2	146	75.00	3.33	–	878.32	4.77

Table 5 (continued)

No	Peak strength of unconfined concrete, f_c (MPa)	AFRP properties			Geometrical properties						Experimental results	FEA results	% Increase vs unconfined
		No. of layers	Thickness of single layer (mm)	Total thickness, t_f (mm)	Diameter of column, D (mm)	Height of column, H (mm)	Thickness of aluminum tube, t_{al} (mm)	Diameter of concrete core, D_c (mm)	D/t	H/D	Ultimate load (kN)	Ultimate load (kN)	
27	30	5	0.2	1	150	500	2	146	75.00	3.33	–	997.88	19.05
28	30	7	0.2	1.4	150	500	2	146	75.00	3.33	–	1177.84	40.53
29	30	0	0	0	150	500	4	142	37.50	3.33	–	1196.57	–
30	30	1	0.2	0.2	150	500	4	142	37.50	3.33	–	1173.48	− 1.93
31	30	3	0.2	0.6	150	500	4	142	37.50	3.33	–	1211.83	1.28
32	30	5	0.2	1	150	500	4	142	37.50	3.33	–	1327.85	10.97
33	30	7	0.2	1.4	150	500	4	142	37.50	3.33	–	1509.03	26.11
34	30	0	0	0	150	500	8	134	18.75	3.33	–	1645.30	–
35	30	1	0.2	0.2	150	500	8	134	18.75	3.33	–	1579.28	− 4.01
36	30	3	0.2	0.6	150	500	8	134	18.75	3.33	–	1645.14	− 0.01
37	30	5	0.2	1	150	500	8	134	18.75	3.33	–	1762.90	7.15
38	30	7	0.2	1.4	150	500	8	134	18.75	3.33	–	1924.07	16.95
39	30	0	0	0	300	500	2	296	150.00	1.67	–	2565.03	–
40	30	1	0.2	0.2	300	500	2	296	150.00	1.67	–	2574.22	0.36
41	30	3	0.2	0.6	300	500	2	296	150.00	1.67	–	2590.71	1.00
42	30	5	0.2	1	300	500	2	296	150.00	1.67	–	2630.25	2.54
43	30	7	0.2	1.4	300	500	2	296	150.00	1.67	–	2761.61	7.66
44	30	0	0	0	300	500	4	292	75.00	1.67	–	3355.54	–
45	30	1	0.2	0.2	300	500	4	292	75.00	1.67	–	3306.51	− 1.46
46	30	3	0.2	0.6	300	500	4	292	75.00	1.67	–	3334.50	− 0.63
47	30	5	0.2	1	300	500	4	292	75.00	1.67	–	3376.12	0.61
48	30	7	0.2	1.4	300	500	4	292	75.00	1.67	–	3509.89	4.60
49	30	0	0	0	300	500	8	284	37.50	1.67	–	4786.14	–
50	30	1	0.2	0.2	300	500	8	284	37.50	1.67	–	4580.85	− 4.29
51	30	3	0.2	0.6	300	500	8	284	37.50	1.67	–	4622.51	− 3.42

Table 5 (continued)

No	Peak strength of unconfined concrete, f_c (MPa)	AFRP properties			Geometrical properties						Experimental results	FEA results	% Increase vs unconfined
		No. of layers	Thickness of single layer (mm)	Total thickness, t_f (mm)	Diameter of column, D (mm)	Height of column, H (mm)	Thickness of aluminum tube, t_{al} (mm)	Diameter of concrete core, D_c (mm)	D/t	H/D	Ultimate load (kN)	Ultimate load (kN)	
52	30	5	0.2	1	300	500	8	284	37.50	1.67	–	4670.72	− 2.41
53	30	7	0.2	1.4	300	500	8	284	37.50	1.67	–	4815.08	0.60
54	50	0	0	0	150	500	2	146	75.00	3.33	–	1167.29	–
55	50	1	0.2	0.2	150	500	2	146	75.00	3.33	–	1174.36	0.61
56	50	3	0.2	0.6	150	500	2	146	75.00	3.33	–	1202.27	2.99
57	50	5	0.2	1	150	500	2	146	75.00	3.33	–	1320.29	13.10
58	50	7	0.2	1.4	150	500	2	146	75.00	3.33	–	1499.07	28.43
59	50	0	0	0	150	500	4	142	37.50	3.33	–	1469.65	–
60	50	1	0.2	0.2	150	500	4	142	37.50	3.33	–	1475.36	0.39
61	50	3	0.2	0.6	150	500	4	142	37.50	3.33	–	1510.91	2.81
62	50	5	0.2	1	150	500	4	142	37.50	3.33	–	1636.05	11.32
63	50	7	0.2	1.4	150	500	4	142	37.50	3.33	–	1814.39	23.45
64	50	0	0	0	150	500	8	134	18.75	3.33	–	1954.35	–
65	50	1	0.2	0.2	150	500	8	134	18.75	3.33	–	1896.06	− 2.98
66	50	3	0.2	0.6	150	500	8	134	18.75	3.33	–	1942.82	− 0.59
67	50	5	0.2	1	150	500	8	134	18.75	3.33	–	2062.09	5.51
68	50	7	0.2	1.4	150	500	8	134	18.75	3.33	–	2222.36	13.72
69	50	0	0	0	300	500	2	296	150.00	1.67	–	3913.49	–
70	50	1	0.2	0.2	300	500	2	296	150.00	1.67	–	3921.38	0.20
71	50	3	0.2	0.6	300	500	2	296	150.00	1.67	–	3936.19	0.58
72	50	5	0.2	1	300	500	2	296	150.00	1.67	–	3974.52	1.56
73	50	7	0.2	1.4	300	500	2	296	150.00	1.67	–	4105.39	4.90
74	50	0	0	0	300	500	4	292	75.00	1.67	–	4679.18	–
75	50	1	0.2	0.2	300	500	4	292	75.00	1.67	–	4677.98	− 0.03
76	50	3	0.2	0.6	300	500	4	292	75.00	1.67	–	4692.73	0.29

Table 5 (continued)

No	Peak strength of unconfined concrete, f_c (MPa)	AFRP properties			Geometrical properties						Experimental results	FEA results	% Increase vs unconfined
		No. of layers	Thickness of single layer (mm)	Total thickness, t_f (mm)	Diameter of column, D (mm)	Height of column, H (mm)	Thickness of aluminum tube, t_{al} (mm)	Diameter of concrete core, D_c (mm)	D/t	H/D	Ultimate load (kN)	Ultimate load (kN)	
77	50	5	0.2	1	300	500	4	292	75.00	1.67	–	4733.33	1.16
78	50	7	0.2	1.4	300	500	4	292	75.00	1.67	–	4865.24	3.98
79	50	0	0	0	300	500	8	284	37.50	1.67	–	5887.43	–
80	50	1	0.2	0.2	300	500	8	284	37.50	1.67	–	5851.17	− 0.62
81	50	3	0.2	0.6	300	500	8	284	37.50	1.67	–	5897.79	0.18
82	50	5	0.2	1	300	500	8	284	37.50	1.67	–	5952.05	1.10
83	50	7	0.2	1.4	300	500	8	284	37.50	1.67	–	6093.87	3.51
84	70	0	0	0	150	500	2	146	75.00	3.33	–	1496.80	–
85	70	1	0.2	0.2	150	500	2	146	75.00	3.33	–	1503.06	0.42
86	70	3	0.2	0.6	150	500	2	146	75.00	3.33	–	1529.99	2.22
87	70	5	0.2	1	150	500	2	146	75.00	3.33	–	1647.51	10.07
88	70	7	0.2	1.4	150	500	2	146	75.00	3.33	–	1825.76	21.97
89	70	0	0	0	150	500	4	142	37.50	3.33	–	1775.11	–
90	70	1	0.2	0.2	150	500	4	142	37.50	3.33	–	1782.68	0.43
91	70	3	0.2	0.6	150	500	4	142	37.50	3.33	–	1815.15	2.26
92	70	5	0.2	1	150	500	4	142	37.50	3.33	–	1936.27	9.08
93	70	7	0.2	1.4	150	500	4	142	37.50	3.33	–	2112.52	19.01
94	70	0	0	0	150	500	8	134	18.75	3.33	–	2186.31	–
95	70	1	0.2	0.2	150	500	8	134	18.75	3.33	–	2144.34	− 1.92
96	70	3	0.2	0.6	150	500	8	134	18.75	3.33	–	2187.63	0.06
97	70	5	0.2	1	150	500	8	134	18.75	3.33	–	2298.55	5.13
98	70	7	0.2	1.4	150	500	8	134	18.75	3.33	–	2458.68	12.45
99	70	0	0	0	300	500	2	296	150.00	1.67	–	5277.75	–
100	70	1	0.2	0.2	300	500	2	296	150.00	1.67	–	5285.68	0.15
101	70	3	0.2	0.6	300	500	2	296	150.00	1.67	–	5300.48	0.43

Table 5 (continued)

No	Peak strength of unconfined concrete, f_c (MPa)	AFRP properties			Geometrical properties						Experimental results	FEA results	% Increase vs unconfined
		No. of layers	Thickness of single layer (mm)	Total thickness, t_f (mm)	Diameter of column, D (mm)	Height of column, H (mm)	Thickness of aluminum tube, t_{al} (mm)	Diameter of concrete core, D_c (mm)	D/t	H/D	Ultimate load (kN)	Ultimate load (kN)	
102	70	5	0.2	1	300	500	2	296	150.00	1.67	–	5338.94	1.16
103	70	7	0.2	1.4	300	500	2	296	150.00	1.67	–	5470.29	3.65
104	70	0	0	0	300	500	4	292	75.00	1.67	–	6005.38	–
105	70	1	0.2	0.2	300	500	4	292	75.00	1.67	–	6016.21	0.18
106	70	3	0.2	0.6	300	500	4	292	75.00	1.67	–	6034.87	0.49
107	70	5	0.2	1	300	500	4	292	75.00	1.67	–	6075.75	1.17
108	70	7	0.2	1.4	300	500	4	292	75.00	1.67	–	6206.69	3.35
109	70	0	0	0	300	500	8	284	37.50	3.33	–	7100.50	–
110	70	1	0.2	0.2	300	500	8	284	37.50	3.33	–	7092.31	− 0.12
111	70	3	0.2	0.6	300	500	8	284	37.50	3.33	–	7130.03	0.42
112	70	5	0.2	1	300	500	8	284	37.50	3.33	–	7187.47	1.22
113	70	7	0.2	1.4	300	500	8	284	37.50	3.33	–	7325.61	3.17

Author contribution D.Q. writing, modelling and analysis S.A. writing, modelling and analysis A.K. writing, modelling and analysis P.S. writing, modelling and analysis S.S. writing, modelling and analysis R.A writing and Review.

Data availability No datasets were generated or analysed during the current study.

Declarations

Competing interest The authors declare no competing interests.

Open Access This article is licensed under a Creative Commons Attribution 4.0 International License, which permits use, sharing, adaptation, distribution and reproduction in any medium or format, as long as you give appropriate credit to the original author(s) and the source, provide a link to the Creative Commons licence, and indicate if changes were made. The images or other third party material in this article are included in the article's Creative Commons licence, unless indicated otherwise in a credit line to the material. If material is not included in the article's Creative Commons licence and your intended use is not permitted by statutory regulation or exceeds the permitted use, you will need to obtain permission directly from the copyright holder. To view a copy of this licence, visit http://creativecommons.org/licenses/by/4.0/.

References

ABAQUS (2017) Standard User's Manual, Version 6.17, D. S. s. S. Corp., USA

Abdalla KM, Al-Rousan R, Alhassan MA, Lagaros ND (2020) Finite-element modelling of concrete-filled steel tube columns wrapped with CFRP. Proc Inst Civ Eng-Struct Build 173(11):844–857

Al-Rousan R (2020) Behavior of circular reinforced concrete columns confined with CFRP composites. Procedia Manuf 44:623–630

Al-Rousan RZ (2022) Cyclic lateral behavior of NLFEA heat-damaged circular CFT steel columns confined at the end with CFRP composites. Case Stud Constr Mater 17:e01223

Al-Rousan RZ, Alnemrawi BAR (2023) Cyclic behavior of CFRP confined circular CFST damaged by alkali-silica reaction. Int J Civil Eng 21(7):1159–1180

Al-Rousan RZ, Bara'a RA (2025) Impact of column axial load level of the seismic behavior of concrete-filled UHPC tubular column-to-footing connections reinforced with different spiral stirrup spacing. Results Eng 26:104952

Al-Rousan RZ, Barfed MH (2019) Impact of curvature type on the behavior of slender reinforced concrete rectangular column confined with CFRP composite. Compos Part B Eng 173:106939

Al-Rousan R, Nusier O, Abdalla K, Alhassan M, Lagaros ND (2022) NLFEA of sulfate-damaged circular CFT steel columns confined with CFRP composites and subjected to axial and cyclic lateral loads. Buildings 12(3):296

Al-Rousan RZ, Bara'a RA, Sawalha HM (2024) The ultimate capacity of geopolymer recycled aggregate concrete filled steel tubular columns: numerical and theoretical study. J Build Eng 96:110365

Al-Sulayvani BJ, Al-Talabani DN (2015) Strengthening and repair of circular RC slabs with openings using CFRP strips under repeated loading. Constr Build Mater 84:73–83

Amir M, Papakonstantinou K, Warn G (2022) State-space formulation for structural analysis with coupled degradation-plasticity and geometric nonlinearity. J Struct Eng 148(4):04022016

Building Code Requirements for Structural Concrete and Commentary (2019) ACI-318M-19, USA

Chen Z, Xu W, Zhou J (2022) Mechanical performance of marine concrete filled CFRP-aluminum alloy tube columns under axial compression: experiment and finite element analysis. Eng Struct 272:114993

Desayi P, Krishnan S (1964) Equation for the stress-strain curve of concrete. J Proc 61(3):345–350

Ding F et al (2021) Numerical investigation of the composite action of axially compressed concrete-filled circular aluminum alloy tubular stub columns. Materials 14(9):2435

Djerrad A, Fan F, Zhi X, Wu Q (2024) Experimental and numerical studies on AFRP-reinforced thin-walled tubes under axial impact loading. Int J Impact Eng 190:104974

Ellobody E, Young B, Lam D (2006) Behaviour of normal and high strength concrete-filled compact steel tube circular stub columns. J Constr Steel Res 62(7):706–715

Farooq U et al (2024) Towards sustainable construction: harnessing potential of pumice powder for eco-friendly concrete, augmented by hybrid fiber integration to elevate concrete performance. Case Stud Constr Mater 21:e03815

Fediuk R et al (2023) Combined effect on properties and durability performance of nanomodified basalt fiber blended with bottom ash-based cement concrete: ANOVA evaluation. J Market Res 23:2642–2657

Hakeem IY, Mansour W, Li W, Badawi M (2024) Analyze the potential for employing internally welded steel plates to improve the shear response of high-strength self-compacting concrete-encased steel beams with large web openings. Eng Struct 304:117636

Hu H-T, Huang C-S, Wu M-H, Wu Y-M (2003) Nonlinear analysis of axially loaded concrete-filled tube columns with confinement effect. J Struct Eng 129(10):1322–1329

Hu H-T, Huang C-S, Wu M-H, Wu Y-M (2002) Numerical analysis of concrete-filled steel tubes subjected to axial force. In: ISOPE international ocean and polar engineering conference. ISOPE, pp ISOPE-I-02-401

Jiang M, Shu Q, Liu P, Wang F, Zhu M, Wang W (2024a) Testing and numerical simulation of concrete-filled 6061-T6 aluminum tubular stub columns. In: Structures. Elsevier, Amsterdam, vol 60, p 105855

Jiang M, Shu Q, Yuan G, Wu J, Wang F (2024b) Compressive testing and numerical modelling of concrete-filled aluminium tubular stub columns after exposure to high temperatures. In: Structures. Elsevier, Amsterdam, vol 70, p 107523

Joyklad P et al (2024) Structural behavior of RC one-way slabs strengthened with ferrocement and FRP composites. Eng Fail Anal 161:108328

Kandiri A, Shakor P, Kurda R, Deifalla AF (2022) Modified artificial neural networks and support vector regression to predict lateral pressure exerted by fresh concrete on formwork. Int J Concr Struct Mater 16(1):1–22

Kandiri A, Ghiasi R, Nogal M, Teixeira R (2024) Travel time prediction for an intelligent transportation system based on a data-driven feature selection method considering temporal correlation. Transp Eng 18:100272

Li G, Zhan Z, Yang Z, Fang C, Yang Y (2020) Behavior of concrete-filled square steel tubular stub columns stiffened with encased I-section CFRP profile under biaxial bending. J Constr Steel Res 169:106065

Lu Y et al (2024) Comparative analysis of shear behavior and mechanism of concrete beams with strip-shaped CFRP or conventional steel stirrups. Case Stud Constr Mater 20:e03140

Lundberg SM, Lee S-I (2017) A unified approach to interpreting model predictions. In: Advances in neural information processing systems, vol 30

Mander JB, Priestley MJ, Park R (1988) Theoretical stress-strain model for confined concrete. J Struct Eng 114(8):1804–1826

Mansour W, Fayed S, Basha A (2022) Experimental and numerical analysis of the punching behavior of RC isolated footings. Steel Compos Struct 45(5):665–682

Mansour W et al (2024a) Improving the flexural response of timber beams using externally bonded carbon fiber-reinforced polymer (CFRP) sheets. Materials 17(2):321

Mansour W, Osama B, Li W, Wang P, Sobuz MHR (2024b) Numerical response of concrete-filled steel tubular (CFST) columns externally strengthened with FRP composites subjected to cyclic loading. Int J Concr Struct Mater 18(1):82

Mi Q, Shu Q, Wang F, Liu P, Zhu M, Wang W (2024) Experimental study on eccentric compressive behaviors of 6061–T6 aluminum tubular long columns filled with concrete. Eng Struct 299:117040

Molnar C (2020) Interpretable machine learning. Lulu. com

Qader DN, Sirwan R, Ali MK (2024) Impact of composite and aluminium face sheets on the properties of the 3D-printed cores under quasi-static three-point bending. Electron J Struct Eng 24(1):12–15

Richart FE, Brandtzæg A, Brown RL (1928) A study of the failure of concrete under combined compressive stresses. University of Illinois. Engineering Experiment Station. Bulletin; no. 185

Rodsin K, Ejaz A, Hussain Q, Parichatprecha R (2023) Experimental and analytical studies on low-cost glass-fiber-reinforced-polymer-composite-strengthened reinforced concrete beams: a comparison with carbon/sisal fiber-reinforced polymers. Polymers 15(19):4027

Rong B, Zhai X, Li Z, Cheng H, Dong A, Zhang R (2023) Study on axial compression behavior of 7A04-T6 concrete-filled aluminum tubular columns. J Build Eng 76:107118

Saha A, Tonmoy TM, Sobuz MHR, Aditto FS, Mansour W (2024) Assessment of mechanical, durability and microstructural performance of sulphate-resisting cement concrete over portland cement in the presence of salinity. Constr Build Mater 420:135527

Saingam P, Hussain Q, Sua-Iam G, Nawaz A, Ejaz A (2024) Hemp fiber-reinforced polymers composite jacketing technique for sustainable and environment-friendly concrete. Polymers 16(13):1774

Saingam P et al (2025) Influence of recycled electronic waste fiber on the mechanical and durability characteristics of eco-friendly self-consolidating mortar incorporating recycled glass aggregate. Case Stud Constr Mater 22:e04369

Suparp S et al (2023) Behavior of non-prismatic RC beams with conventional steel and green GFRP rebars for sustainable infrastructure. Sci Rep 13(1):15733

Talpur SA et al (2024) Machine learning approach to predict the strength of concrete confined with sustainable natural FRP composites. Compos Part c: Open Access 14:100466

Tang H, Chen J, Fan L, Sun X, Peng C (2020) Experimental investigation of FRP-confined concrete-filled stainless steel tube stub columns under axial compression. Thin-Walled Struct 146:106483

Tao Z, Wang Z-B, Yu Q (2013) Finite element modelling of concrete-filled steel stub columns under axial compression. J Constr Steel Res 89:121–131

Thansirichaisree P, Mohamad H, Ejaz A, Saingam P, Hussain Q, Suparp S (2024) Stress-strain behavior of square concrete columns confined with hybrid B-CSM composites and development of novel prediction models. Compos Part c: Open Access 14:100448

Wang F-C, Zhao H-Y, Han L-H (2019) Analytical behavior of concrete-filled aluminum tubular stub columns under axial compression. Thin-Walled Struct 140:21–30

Wang Y, Cai G, Larbi AS, Waldmann D, Tsavdaridis KD, Ran J (2020) Monotonic axial compressive behaviour and confinement mechanism of square CFRP-steel tube confined concrete. Eng Struct 217:110802

Wang M, Tang C, Qiu Q, Yu Y (2023) Experimental study and numerical analysis on axial compression of round-ended concrete filled CFRP-aluminum tube columns. PLoS ONE 18(12):e0296005

Wang Y et al (2025) Modeling of concrete-filled PVC tube columns confined with CFRP strips under uniaxial eccentric compression: machine learning and finite element approaches. J Big Data 12(1):34

Yan XF, Ahmed M, Hassanein M, He MN (2023) Performance analysis and design of circular high-strength concrete-filled double-skin aluminum tubular short columns under axial loading. Struct Concr 24(5):5677–5696

Yan X-F, Hao J-P, He M-N (2024a) Behavior of circular concrete-filled double-skin aluminum alloy tubular stub columns: test, modeling and confinement-based design. J Build Eng 95:110060

Yan X-F, Lin S, Zhao Y-G (2024b) Behaviour and confinement mechanism of circular concrete-filled aluminum alloy tubular stub columns under axial compression. Mar Struct 95:103600

Yan X-F, He M-N, Hao J-P, Lin S (2024c) Theoretical model of circular concrete-filled aluminum alloy tubular short columns under axial compression. Eng Struct 303:117549

Yooprasertchai E et al (2024) Sustainable development of concrete through treated and untreated plastic waste aggregates. Sci Rep 14(1):22051

Yue C et al (2024) Utilization finite element and machine learning methods to investigation the axial compressive behavior of elliptical FRP-confined concrete columns. In: Structures. Elsevier, vol 70, p 107681

Zhang S, Miao K, Wei Y, Xu X, Luo B, Shi W (2023) Experimental and theoretical study of concrete-filled steel tube columns strengthened by FRP/steel strips under axial compression. Int J Concr Struct Mater 17(1):1

Zhou F, Young B (2008) Tests of concrete-filled aluminum stub columns. Thin-Walled Struct 46(6):573–583

Zhou F, Young B (2009) Concrete-filled aluminum circular hollow section column tests. Thin-Walled Struct 47(11):1272–1280

Zhou F, Young B (2012) Numerical analysis and design of concrete-filled aluminum circular hollow section columns. Thin-Walled Struct 50(1):45–55

Zhou F, Young B (2018) Concrete-filled double-skin aluminum circular hollow section stub columns. Thin-Walled Struct 133:141–152

Zhu J-H, Young B (2006) Aluminum alloy tubular columns—Part I: finite element modeling and test verification. Thin-Walled Struct 44(9):961–968

Publisher's Note Springer Nature remains neutral with regard to jurisdictional claims in published maps and institutional affiliations.